DTU Library

Effects of electrolyte anion adsorption on the activity and stability of single atom electrocatalysts

Patniboon, Tipaporn; Hansen, Heine Anton

Published in:
Chemical Physics Reviews

Link to article, DOI:
10.1063/5.0125654

Publication date:
2023

Document Version
Peer reviewed version

Citation (APA):
Patniboon, T., & Hansen, H. A. (2023). Effects of electrolyte anion adsorption on the activity and stability of single atom electrocatalysts. *Chemical Physics Reviews*, *4*(1), Article 011401. https://doi.org/10.1063/5.0125654

Effects of Electrolyte Anion Adsorption on the Activity and Stability of Single Atom Electrocatalysts

Tipaporn Patniboon and Heine Anton Hansen
Department of Energy Conversion and Storage, Technical University of Denmark
Anker Engelunds Vej, 2800 Kongens Lyngby, Denmark

ABSTRACT

A single metal site incorporated in N-doped carbon (M/N/C) is a promising electrocatalyst. Here, we perform a computation investigation of the effect of electrolyte anion adsorption on the activity and stability of single-atom catalysts (MN_4) with M as transition metal and p-block metal. The MN_4 site on two different graphene structures (bulk graphene and graphene edge) is studied under electrochemical conditions for the oxygen reduction reaction (ORR) and the CO_2 reduction reaction (CO_2RR). Because of the two-dimensional nature of the catalyst, reaction intermediates and electrolyte ions can interact with both sides of the single-atom catalyst. As a result, the electrolyte anions compete with water and adsorbate on the single metal site, in some cases either poisoning or modifying the catalyst activity and thermodynamic stability. We find most electrolyte anions adsorbs on the single metal site under ORR conditions but not at the lower potentials for the CO_2RR. Still, the adsorption of water and gas molecules can occur under CO_2RR conditions. For example, under ORR conditions, the thermodynamic driving force of the $*SO_4$-FeN_4 site in the 0.1 M H_2SO_4 solution is about 0.47-0.56 eV lower than the *O-FeN_4 site in water, depending on the local carbon structure. Additionally, the stabilization by electrolyte anions depends on the nature of the metal atom. Our study demonstrates the important role of electrolytes and the coordination environment for the activity and stability of the M/N/C catalyst.

INTRODUCTION

Single metal atom coordinated N-doped carbon (M/N/C) has been recognized as an efficient electrocatalyst. Compared to the bulk metal, the single-atom catalyst maximizes the metal atom utilization, thus exhibiting impressively high activity and selectivity. In many experimental and theoretical studies, the Fe/N/C and Co/N/C materials have been identified as active ORR catalysts in acid electrolytes[1–5]. More recent studies showed that the M/N/C catalyst is also an efficient catalyst for the CO_2RR[6–8]. The metal centers are crucial for the reaction, and the MN_y site is suggested as the active site for the ORR[4] and CO_2RR[6]. In addition, the coordination environment is suggested to play an important role in both catalytic activity and stability[7,8]. Many studies have been made to determine the detailed structure and map the relationship between catalyst structure, activity, and stability. Many structures of the MN_4 site with different local carbon structures (i.e., MN_4C_8[3,9,10], MN_4C_{10}[8,11], MN_4C_{12}[2,4,14], edged-hosted MN_4[12–14]) have been proposed from experimental and theoretical studies. Still, there is a wide debate about the active and stable site in the M/N/C materials.[8,15–21]

Additionally, possessing two-dimensional structures, the M/N/C catalyst is distinct from the bulk materials, where only one exposed side is responsible for its catalytic activity. Ideally, both sides of the M/N/C catalyst are exposed to electrolyte so both sides can interact with an adsorbate. An electrolyte anion or a gas molecule from the environment may adsorb on one side of the MN_y site while the other side is still available for the reaction to proceed.[22,23] The presence of the adsorbate on one side of the single metal atom will modify its electronic states, affecting the binding of the second adsorbate on the other side[24,25]. Combining in situ extended X-ray absorption fine structure (EXAFS), X-ray absorption near edge structure (XANES), and the density functional theory (DFT) calculations, Jia *et al*. reported that the active site in Fe/N/C catalysts undergoes the Fe^{2+}/Fe^{3+} redox transition associated with the adsorption of *OH through the water[26]. Also, they have suggested that the *OH may serve as a fifth ligand responsible for the high ORR activity[26]. Previous DFT calculations by Holby *et al*. point to the possible enhancements in the ORR activity of the FeN_4 site on the graphene by an OH ligand from the spontaneous decomposition of water[14,27,28]. Many experimental and theoretical studies have already considered the effect of the ligand from the electrolyte or a gas molecule impurity, e.g., NH_3, NH_2, OH, CN, SO_3, and pyridine on ORR activity, and suggested that the ligand can modify the ORR activity of the M/N/C cattalyst[13,14,22–24,27,29–39]. For instance, Holst-Olesen *et al*. found that the presence of anions from H_3PO_4 or CH_3COOH-containing electrolytes is beneficial for the ORR activity on the Fe/N/C catalyst[22,23]. Various combinations of the electrolyte anion ligand and the single metal center in the MN_4C_{12} structure (M = Cr, Mn, Fe, and Co) for improving the ORR activity have also been suggested in a previous theoretical study by Svane *et al*.[24] Recently, studies have also reported that the introduction of axial oxygen[40,41] or halogen atom[25] on the MN_4C structure can achieve an efficient catalyst for the CO_2RR.

Besides the catalytic activity, the stability of the MN_4 site with the presence of a fifth ligand was recently discussed. Glibin *et al*. have previously studied the dissolution reaction of two different FeN_4 sites with *F ligand based on a thermodynamic model and suggested that the fluorination on the FeN_4 sites increases the resistance of the single metal site against acid leaching[42]. Density functional theory (DFT) calculations have been used to study the dissolution reaction of the FeN_4 site embedded on a bilayer-graphene by Holby *et al*. [19] This study has suggested the presence of *OH ligand on the FeN_4C_{10} site thermodynamically prevents the single Fe metal site from dissolution[19]. Using in situ Raman spectroscopy of molecule Fe phthalocyanine (FePc) model and pyrolyzed Fe/N/C catalyst, Wei *et al*. have reported the structural dynamics of the FeN_4 active site in acid solution (0.1 M $HClO_4$). At high potential (1.0 V_{RHE}), a non-planar structure is induced by an adsorbate on the FeN_4 site, and the structure is stable against dissolution. In contrast, the irreversible attenuation of the planar Fe-N vibration after staying at a lower potential for a long time (at 0.05 V_{RHE} for 15 min) has been suggested as evidence for the dissolution of the Fe center[43]. Using DFT simulations with ^{57}Fe Mössbaur spectroscopy data, Nematollahi et al. have compared the DFT calculated and experimental quadrupole splitting energy of doublets (ΔE_{QS}) for different FeN_4 structures (FeN_4C_{10}, FeN_4C_{12}, FeN_4C_8) both with and without ligands. They have suggested the FeN_4C_8 structure with a fifth ligand such as OH^- and NH_2^- could be an active and durable site for the ORR in acid conditions[20].

Here, we systematically explore the effect of electrolyte anion adsorption on the stability and activity of a single metal atom with N ligands doped into a bulk graphene terrace (MN_4C_{10}) and a graphene edge (MN_4C_A) with M = 3d, 4d, 5d, or p-block (Sn, Sb, and Bi) metal atoms. These graphene sites are selected because they are among the most stable sites[18]. We determine the interaction between the single metal site with the electrolyte anion and evaluate how the electrolyte adsorption thermodynamically influences the dissolution of the single metal site under electrochemical conditions relevant to the ORR and CO_2RR. We then investigate the catalytic activity with the presence of an electrolyte anion ligand for the ORR and CO_2RR. Finally, the results are used to suggest combinations of a metal atom, local carbon structure, and electrolyte for active and stable catalysts under working conditions. We show how the chemical environment around the single-atom site plays a crucial role in determining the activity and stability of the catalyst.

RESULTS AND DISCUSSION

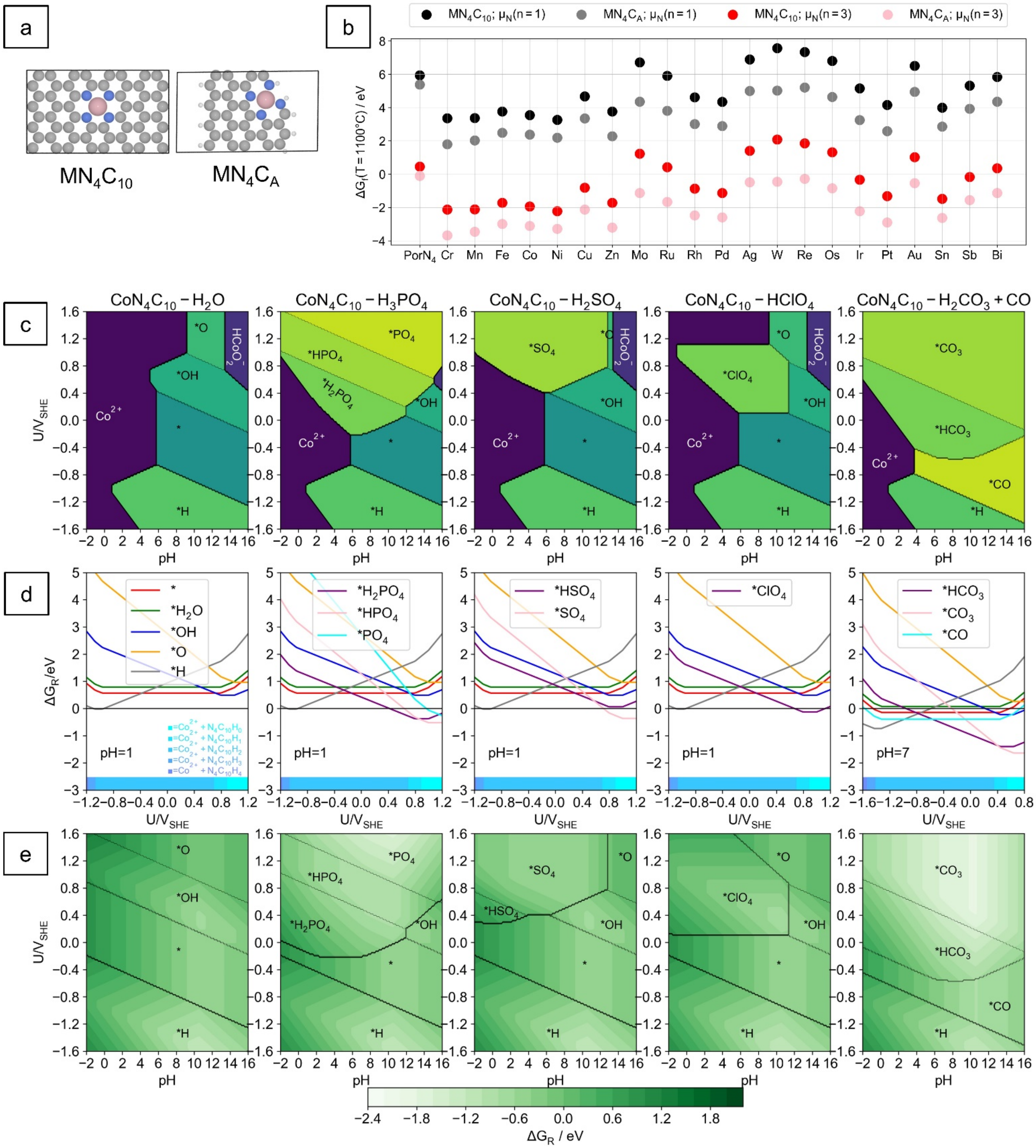

Figure 1 (a) Single atom site in bulk graphene (MN_4C_{10}) and a graphene edge (MN_4C_A) (C = grey, N = blue, H = white, M = pink). (b) ΔG_f for MN_4C_{10} and MN_4C_A sites. (c) Stability diagrams for the CoN_4C_{10} site

in 0.1 M solutions. (d) ΔG_R for the sites at specific pH and (e) Stability diagrams for the CoN_4C_{10} site showing the most stable surface.

Here we consider the structural models of the MN_4C_{10} and MN_4C_A sites, as shown in **Figure 1 (a)**. The MN_4C_{10} site was previously reported as a durable site in acid[8,18,44]. Also, the MN_4C_A site, which represents the MN_4 site at the armchair edge, is included since it was previously found to be a stable and active site for the ORR under acid conditions[18,45]. We calculate the formation free energy of the single metal atom doped into bulk graphene and the graphene edge as follows:

$$\Delta G_f = E(MN_4C) - (E(C) - 6\mu_C - \mu_M - 4\mu_N) \qquad \text{Equation 1}$$

$E(MN_4C)$ is the total energy of the single metal atom doped into graphene. $E(C)$ is the total energy of a pristine graphene sheet or pristine graphene nanoribbon. μ_C is the total energy of the pristine graphene sheet per carbon atom. μ_M is the total energy of metal in its bulk structure per metal atom. The nitrogen chemical potential (μ_N) is treated as a parameter for the use of different nitrogen precursors in experiments[11,46–51]. μ_N is referenced to NH_3, N_2, and H_2 at 1 bar and can be expressed as $\mu_N(n) = n[G(NH_3) - (3/2)G(H_2)] + (1/2)(1 - n)G(N_2)$ where n is an integer. Thus, when n = 0, the nitrogen reference source is the N_2 gas molecule at 1 bar, and when n = 1, the nitrogen reference source is the NH_3 gas molecule. The nitrogen chemical potential can vary as a function of N_2, H_2, and NH_3 content in the environment gas during the synthesis. The $n < 0$ situation corresponds to synthesis under the high pressure of $N_2 + H_2$, and the $n > 1$ situation corresponds to the synthesis under the high pressure of NH_3.

Figure 1 (b) shows the ΔG_f of MN_4C_{10} and MN_4C_A at two different $\mu_N(n)$ with n=1,3. The temperature is considered at T=1100 ℃, a typical condition for the M/N/C synthesis[4,52,53]. Regardless of the metal atom and $\mu_N(n)$, the single atom site is thermodynamically preferred to form at the graphene edge over bulk graphene, in agreement with the previous studies, which have also suggested a lower formation energy; thus, a higher relative stability for the MN_y site at the edged than the basal plane[12,45,54,55]. We find that a pyridine vacancy ($PorN_4$) is more stable on the graphene edge than the bulk graphene, and it is likely to be further stabilized if the bulk metal atom is supplied, forming the MN_4 site. Most 3d elements are more favorable to dope into the pyridine vacancy than the 4d-5d elements and p-elements. The formation becomes thermodynamic favorable when n increase from 1 to 3 (e.g., under the elevated NH_3 partial pressure) at T=1100 ℃. Figure S1 (b) shows that the nitrogen chemical potential changes with temperature. Thus, the formation free energies depend on temperature and the nitrogen chemical potential. Let us consider the formation free energy of the CoN_4C_{10} site as an example, as shown in **Figure S1 (c)**. Increasing temperature makes the formation more favorable when $n > 1$. In other words, the synthesis under the high NH_3 partial pressure and high temperature (T > 500 ℃) is favorable for the single atom formation. At low temperatures (T < 100 ℃), the formation becomes thermodynamic favorable when $n < 0$ (e.g., under high N_2+H_2 content). **Figure S2** shows the formation free energy of all considered MN_4 structures at T=25℃ and 1100 ℃ as a function of μ_N, suggesting that the considered single metal sites doped into graphene can be synthesized in a controlled experiment.

We then consider the stability of the MN_4 site in an electrochemical environment where the single metal atom can interact with anions from the electrolyte or reaction intermediates. We consider anions from commonly used electrolytes for the ORR or the CO_2RR[56–58], e.g., $H_2PO_4^-$, HPO_4^{2-}, PO_4^{3-} in H_3PO_4 solution; HSO_4^-, SO_4^{2-} in H_2SO_4 solution; Cl^- in HCl solution; ClO_4^- in $HClO_4$ solution; NO_3^- in HNO_3 solution; HCO_3^- and CO_3^{2-} in H_2CO_3 solution. Furthermore, NO and CO gas molecules and CN^- in HCN solution are included as they have been found to affect the ORR activity and be used as an effective probe molecule for the active site[59–65]. The complete list of the considered electrolyte anion and poisoning gas molecules is given in **Table S2** and **Table S3**. The adsorption of CO and NO on the single metal site considered in this study does not depend on pH and potential. A previous experimental study by Malko et al. found that liquid nitric oxide (NO) and nitrite (NO_2^-) can be used as electrochemical probes for the Fe/N/C catalyst where the ORR activity can be poisoned and recovered via electrochemical stripping[62,63]. Also, Boldrin *et al*. found that the gas phase NO treatment poisons the Fe/N/C catalyst similarly to liquid phase NO or liquid phase nitrite[64]. Malko *et al*. have suggested that the NO is a poisoning adsorbate that can be stable at the potential between 1.05 – 0.1 V_{RHE}[63]. However, the ORR activity can be recovered by cycling the potential to -0.3 V_{RHE}, where they have suggested that a poisoning species is reductively desorbed. The NO stripping product has been suggested to be ammonium (NH_4^+), associated with transferring 5 electrons per stripping molecule. We considered the possibility of stripping NO from the metal site. More calculation details and results can be found in the supporting information (Section 3). For the FeN_4C_{10} and FeN_4C_A sites, even though we consider the binding of NO on the metal site does not depend on pH and potential, and the NO is found to be thermodynamically stable at the potential from 0.5 to 1.0 V_{SHE} (at pH = 1), the NO stripping is found to be thermodynamically favorable at lower potential ($U < 0.5$ V_{SHE} at pH = 1), suggesting the potential dependence of the NO stripping. The calculation results are qualitatively in line with the experiments by Malko *et al.*[62,63]. The NO stripping potential for other considered MN_4 sites is also calculated and shown in **Figure S4**. Like the FeN_4, the NO striping is thermodynamically favorable at low potential, lower than the potential at which the ORR is expected to be operated (0.8 V_{SHE} at pH = 1). These demonstrate the possibility of using NO as a probe molecule for qualifying ORR active sites for the M/N/C catalyst and having the *NO ligand on the metal site under the ORR.

We consider that the electrolyte anion adsorption on the single metal atom can compete with the water molecule. In each solution, the adsorption of anion or gas molecules on the single metal site competes with forming *OH, *O, and *H from water oxidation or reduction. The adsorption free energy of electrolyte anions is calculated using the thermodynamic cycle[23,24] shown in **Figure S5,** with additional calculation details in **Section 4** of the Supporting Information**.** The change in reaction free energy with an applied potential (U_{SHE}) and pH in this study is calculated using the computational hydrogen electrode (CHE)[66] approach.

Along with the adsorption of the adsorbate, the dissolution of the single metal atom from the graphene host into the electrolyte, resulting in dissolved metal ion (M^{x+}) and the graphene host cavity (N_4CH_n) is considered as follows[19]:

$$MN_4C + nH^+_{(aq)} \rightarrow M^{x+}_{(aq)} + N_4CH_n + (x\text{-}n)e^- \qquad \text{Equation 2}$$

More calculation details about the dissolution reaction can be found in **Section 5** of the supporting information. However, other possible degradation reactions besides the demetalltion[67,68] have been proposed to cause instability of the Fe/N/C catalyst, especially in an acidic environment. These include carbon corrosion[69] and carbon surface oxidation by H_2O_2-derived free radicals[69,70]. These possible degradation mechanisms might coincide and be interrelated[69]. Understanding the degradation mechanism is a prerequisite for the rational design of durable and stable M/N/C catalysts. We believe that the relation between the chemical environment, i.e., electrolyte and local carbon structure around the MN_y site with the demetallation, provides a better understanding of the degradation and is useful for designing intrinsically stable and active catalysts.

For example, **Figure 1 (c)** shows the stability diagram of the CoN_4C_{10} site in 0.1 M solutions. Only the most stable phase at each condition is shown in the stability diagram. It is seen that the electrolyte anion competes with water adsorption and becomes the most favorable adsorbate on a single Co atom.

We further consider the relative stability (ΔG_R), which we define as the free energy difference between the M/N/C catalyst surface (either with or without the adsorbate) and the most stable dissolved species (the dissolved metal ion and carbon host cavity)[47]. Therefore**,** ΔG_R indicates the thermodynamic driving force for the dissolution of the metal atom. The more positive relative stability, the less stable the single metal atom is against dissolution. **Figure 1 (d)** shows ΔG_R as a function of applied potential at specific pH (pH = 1 for H_3PO_4, H_2SO_4, and $HClO_4$ solution and pH = 7 for H_2CO_3+CO solution). The most stable dissolved species for each potential used as a reference for ΔG_R are superimposed as horizontal bars at the bottom in **Figure 1 (d)**. At potentials above 0.6 V_{SHE} and pH = 1, in 0.1 M H_3PO_4, H_2SO_4, and $HClO_4$ solution, it is seen that *HPO_4, *SO_4, and *ClO_4 are thermodynamically preferred on the single Co atom and further reduces the thermodynamic driving force toward dissolution compared to the single Co atom in H_2O. The relative stability of the CoN_4C_A site and the FeN_4 site on both bulk graphene and the graphene edge can be found in **Section 6** of the supplementary information, where similar trends are found. As potential increases, the electrolyte anion becomes thermodynamically stable on the single metal site. Simultaneously, the corresponding thermodynamic driving force becomes lower than the same single metal site in H_2O. Furthermore, it is seen that the thermodynamic driving force toward the dissolution is likely to decrease as the potential increase, suggesting that the demetallation could be dominant at the low potential region in the acid condition. These results are in line with the previous experimental study by Choi *et al*., where the Fe demetallation from the Fe/N/C catalyst in 0.1 M $HClO_4$ was observed at potentials below 0.7 V_{RHE}[68].

At pH = 7 in 0.1 M H_2CO_3 solution with CO[53,58], at potentials below -0.4 V_{SHE}, *H is thermodynamically favorable on the single Co atom. When the potential increases, the anions become the most stable adsorbate on the Co atom (*HCO_3 at potential around -0.6 to 0.4 V_{SHE} and *CO_3 at potential above 0.4 V_{SHE}). As a result, the thermodynamic driving force is lowered by 0.46 eV when the *HCO_3 is stabilized on the Co atom (U = -0.6 to 0.4 V_{SHE}), and it is lowered by 2.18 eV when the *CO_3 is stabilized on the Co atom (U = 0.4 - 1.6 V_{SHE}), compared to the *CO-CoN_4C_{10} site in H_2O+CO solution at the same potential ranges.

The ΔG_R of the most stable MN_4C_{10} and MN_4C_A surface in 0.1 M electrolytes under the ORR condition (pH=1, and U=0.80 V_{SHE}) is shown in **Figure 2(a)** and **Figure S10-S11**. Except for $PtN_4C_{x=10,A}$, $PdN_4C_{x=10,A}$, and $AuN_4C_{x=10,A}$ sites, the other MN_4 sites are likely to be stabilized by the adsorbate. Therefore the thermodynamic driving force is reduced compared to the bare metal site. The $PtN_4C_{x=10,A}$, $PdN_4C_{x=10,A}$, and $AuN_4C_{x=10,A}$ sites weakly interact with electrolyte anions and water molecules. However, they are stable against dissolutions in a wide range of pH and potentials, even without any adsorbate. The stability of the Pt center is consistent with a previous experimental study by Li et al.[71], where a minor change in the current density of a Pt/N/C catalyst under accelerated durability tests in 0.5 M H_2SO_4 has been reported. The relative stability of $IrN_4C_{x=10,A}$ is found to be lower than zero in the considered electrolytes, so it is stable under the considered ORR condition. These results agree with experiments where the Ir/N/C catalyst retains 97% of the current density during a durability test in 0.1 M $HClO_4$[72]. For $CrN_4C_{x=10,A}$, $MoN_4C_{x=10,A}$, $RuN_4C_{x=10,A}$, $ReN_4C_{x=10,A}$, and $OsN_4C_{x=10,A}$ sites, the binding strength of the anion is likely weaker than *O in most considered electrolytes. Thus, these metal sites are covered by *O. According to experimental studies by Zhang et al.[73] and Xiao et al.[74] testing the ORR performance of the Ru/N/C catalyst in 0.1 M $HClO_4$, the active RuN_4 site has been suggested to bond with axial *O or *OH.

Furthermore, a previous experimental study has shown a higher activity loss of the Mn/N/C catalyst than the Fe/N/C catalyst in 0.1 M $HClO_4$ under an accelerated stress test where the potential is cycled between 0.5 and 1.3 V_{RHE}[65]. In agreement with this experiment, in 0.1 M $HClO_4$ in the potential range of 0.5–1.3 V_{RHE} (0.44-1.25 V_{SHE} at pH = 1), we find the thermodynamic driving force toward the dissolution of the MnN_4 site on bulk graphene and graphene edge is about 0.78 eV and 0.57 eV higher than those of the FeN_4 site on bulk graphene and graphene edge, respectively. At U = 0.5–1.0 V_{RHE} in 0.1 M $HClO_4$, the MnN_4 and FeN_4 sites are stabilized by $*ClO_4$. Then, ΔG_R is about 0.25 eV and 0.13 eV lower than in H_2O, respectively. However, in both H_2O and 0.1 M $HClO_4$, the MnN_4 site is found to be less stable than the FeN_4 site.

Another experimental study by Xie et al.[75] has determined the amount of metal leached out from the Fe/N/C and Co/N/C catalyst when the potential is cycled between 0.6–1.0 V_{RHE} in 0.5 M H_2SO_4. They have found a lower amount of metal leaching from the Co/N/C catalyst, compared to the Fe/N/C catalyst, especially when purged with O_2.[75] At U = 0.6–1.0 V_{RHE} (U = 0.55–0.96 V_{SHE} at pH = 1), we find that the FeN_4 and CoN_4 site on both bulk graphene and the graphene edge in 0.1 M H_2SO_4 are occupied by $*SO_4$. The thermodynamic driving force toward the dissolution of the $*SO_4$-CoN_4 site on bulk graphene and graphene edge is about 0.14 eV and 0.13 eV lower than the $*SO_4$-FeN_4 site, agreeing with the experiment. In our previous study[18] where the electrolyte anion adsorption was not included, we found that, at the same condition, the *O-FeN_4 and *OH-CoN_4 is the most stable phase of the FeN_4 and CoN_4 site on both bulk and armchair edge in H_2O. The thermodynamic driving toward the dissolution of the most stable phase of the FeN_4 site on the bulk graphene and graphene edge in H_2O is only 0.04 eV and 0.00 eV higher than the CoN_4 site. These results suggest that our stability calculations, including the electrolyte anion adsorption, compare well with the experimental results for M/N/C catalysts.

For CO adsorption, CO chemisorption experiments on the M/N/C catalyst (M = Fe and Mn) have suggested a stronger CO binding on the Fe-containing site over the Mn-containing site[65]. In agreement with these experiments, we find a stronger CO adsorption on the FeN_4 site than on the MnN_4 site on both bulk graphene and the graphene edge. Similar results have been reported by Svane *et al.*[76] where the MN_4 structure is modeled based on the MN_4C_{12} structure.

In addition, the stability against dissolution is also determined by the local carbon structure. We find that the MN_4 site on the graphene edge is more stable against dissolution than that on the bulk graphene, which is in line with previous studies[18,45]. The thermodynamic driving at U = 0.8 V_{SHE}, pH = 1 of the most stable MN_4 site on the graphene edge is about 0.52 eV lower than those on the bulk graphene, on average.

Since the MN_4 site is embedded in a two-dimensional carbon sheet, the adsorbates may interact with the metal atom from both sides. The electrolyte anion can strongly adsorb on two sides, blocking the metal site from the intermediate adsorbates. Alternatively, if the interaction is weak, the electrolyte anion will adsorb only on one side, allowing the intermediate adsorbates to interact from the other. In the case of weak interaction, i.e., PdN_4C_x, PtN_4C_x, and AuN_4C_x, the bare metal site is responsible for their catalytic activity. In this work, the ORR is considered to proceed through a four-electron associative pathway, and the metal site is considered the active site. Most of the considered MN_4 sites interact with the electrolyte anion under the ORR condition. Thus, the activity of the MN_4 site toward the ORR by considering the following reaction mechanism[23] on the catalyst surface:

$$*A^n/*A^n + ne^- \rightarrow */*A^n + A^{n-} \quad ; \Delta G(ORR)_0 \quad \text{Equation 3}$$

$$*A^n + O_2 + (H^+ + e^-) \rightarrow *OOH/*A^n \quad ; \Delta G(ORR)_1 \quad \text{Equation 4}$$

$$*OOH/*A^n + (H^+ + e^-) \rightarrow *O/*A^n + H_2O \quad ; \Delta G(ORR)_2 \quad \text{Equation 5}$$

$$*O/*A^n + (H^+ + e^-) \rightarrow *OH/*A^n \quad ; \Delta G(ORR)_3 \quad \text{Equation 6}$$

$$*OH/*A^n + (H^+ + e^-) \rightarrow */*A^n + H_2O \quad ; \Delta G(ORR)_4 \quad \text{Equation 7}$$

where $*A^n/*A^n$ is the electrolyte anions (or gas molecules with n = 0) adsorbed on both sides. $*X/*A^n$ stands for the electrolyte anion adsorbs on one side and the reaction intermediate on another, where *X = *O, *OH, *OOH. $\Delta G(*O/*A^n)$ and $\Delta G(*OOH/*A^n)$ are obtained from a scaling relation established for ΔG(*O) vs. ΔG(*OH) and ΔG(*OH) vs. ΔG(*OOH) on the bare metal site (**Figure S14**), respectively. Thus, only $\Delta G(*OH/*A^n)$ is explicitly calculated in this study. The possible electrolyte anion in the reaction is considered the most stable adsorbate at pH = 1 and U = 0.80 V_{SHE}, as shown in Figures 2 (a) and **S10-S11**. The corresponding ORR activity is also calculated at this condition. The change in reaction-free energy with an applied potential (U_{SHE}) and pH is calculated using the computational hydrogen electrode (CHE)[66]. The thermodynamic barrier of the limiting step (ΔG_{max}) along the ORR pathway at pH = 1, U = 0.80 V_{SHE} is the ORR activity descriptor given in **Figure S16-S17**. The limiting potential (U_L) is also calculated if all elementary steps are electrochemical, as shown in **Figure S18-S19**. This includes when NO and CO gas molecules are not thermodynamically stable on both sides of the metal atom.

ORR activity of the FeN_4 site in 0.1 M H_3PO_4, H_2SO_4, $HClO_4$, and HCl is first discussed. At U = 0.8 V_{SHE} and pH = 1, one electrolyte anion (HPO_4^{2-}, SO_4^{2-}, ClO_4^{-}, and Cl^-) bonds with the FeN_4C_{10} and FeN_4C_A sites stronger than the water molecule, so we expected that the electrolyte anion could affect the ORR. **Figure S15** shows free energy diagrams of the ORR on the FeN_4C_{10} and FeN_4C_A sites at U = 0.80 V_{SHE} and pH = 1. The anion removal step limits the ORR on the FeN_4C_{10} site in 0.1 M $HClO_4$ and HCl. In 0.1 H_3PO_4, the thermodynamic barrier of the limiting step is the barrier of the anion removal plus the barrier of the formation *OOH on the FeN_4C_{10} site. While in 0.1 M H_2SO_4, the ORR is limited by the reduction of *OH to H_2O. The lowest ΔG_{max} at U = 0.80 V_{SHE} and pH = 1 for the FeN_4C_{10} site in these electrolytes is found for H_2SO_4 (0.02 eV) < $HClO_4$ (0.13 eV) < H_3PO_4 (0.26 eV) < HCl (0.56 eV). The U_L with the most stable adsorbate at U = 0.80 V_{SHE} and pH = 1 as the ligand on the FeN_4C_{10} site is found in the following order: H_2SO_4 (0.78 V_{SHE}) > $HClO_4$ (0.67 V_{SHE}) > H_3PO_4 (0.60 V_{SHE}) > HCl (0.24 V_{SHE}). These results suggest that the ORR activity of the FeN_4C_{10} site is in the following order: H_2SO_4 > $HClO_4$ > H_3PO_4 > HCl.

For the FeN_4C_A site in 0.1 M H_3PO_4 and HCl, the ORR at U = 0.80 V_{SHE}, and pH = 1 is limited by the anion removal step. In 0.1 M H_2SO_4, the thermodynamic barrier of the limiting step is the barrier of the anion removal plus the formation of *OOH on the FeN_4C_A site. The ORR is limited by the reduction of *OH to H_2O for the FeN_4C_A site in 0.1 M $HClO_4$. The lowest ΔG_{max} at U = 0.80 V_{SHE} and pH = 1 for the FeN_4C_A site in these electrolytes is found to be H_3PO_4 (0.01 eV) < H_2SO_4 (0.08 eV) < $HClO_4$ (0.13 eV) < HCl (0.54 eV). The U_L is found in the following order: H_3PO_4 (0.79 V_{SHE}) > H_2SO_4 (0.76 V_{SHE}) > $HClO_4$ (0.67 V_{SHE}) > HCl (0.26 V_{SHE}). These results suggest that the ORR activity of the FeN_4C_A site is in the following order: H_3PO_4 > H_2SO_4 > $HClO_4$ > HCl. It is seen that the ORR activity obtained from FeN_4C_A and FeN_4C_{10} sites is different, implying a significant role of the local carbon structure around the FeN_4 site in the catalytic activity.

Previous experimental results by Holst-Olesen *et al.*[23] and Hu *et al.*[77] have reported that the ORR activity of the Fe/N/C catalyst in H_3PO_4 is higher than in the other considered electrolytes. Holst-Olesen *et al.*[23] reported the ORR activity in the following order: H_3PO_4 > $HClO_4$ ≈ H_2SO_4 > HCl in 0.5 M electrolyte. At 0.8 V_{RHE}, Hu *et al.*[77] reported the ORR activity of the Fe/N/C catalyst as H_3PO_4 > H_2SO_4 > $HClO_4$ > HCl. Modeling the Fe/N/C catalyst by the FeN_4C_{12} structure, Holst-Olesen *et al.*[23] have reported a good agreement between the theoretical and experimental ORR activity trend. Our calculation results obtained from the FeN_4C_A site agree with the experiments by Hu et al.[77] and Holst-Olesen et al.[23].

Furthermore, both experimental studies by Holst-Olesen *et al.*[23] and Hu *et al.*[77] have suggested a strong poison effect on the Fe/N/C catalyst by Cl^- in HCl solution. In our findings, the thermodynamic barrier of the limiting step in 0.1 M HCl is also higher than in 0.1 M $HClO_4$ and H_2SO_4 solution. Hu *et al.*[77]

have also suggested that the catalytic activity of the Fe/N/C catalyst can be poisoned by ClO_4^- in the $HClO_4$ solution. Our calculation results show that the ClO_4^- can be adsorbed on the FeN_4 site on bulk graphene and graphene edge at U = 0.80 V_{SHE} and pH = 1. The ClO_4^- anions even thermodynamically block the FeN_4C_{10} site at this condition. However, these results disagree with previous theoretical and experimental studies[22,24] based on the MN_4C_{12} (M = Cr, Fe, Mn, Co) structure where the ClO_4^- anion has been found not to adsorb on the MN_4 site at U = 0.75 V in 0.5 M $HClO_4$. Since the structure of pyrolyzed Fe/N/C materials highly depends on the synthetic path and precursor, various FeN_x sites can be formed, and their density can be varied from each experiment. This can be one of the possible reasons for the discrepancy.

Furthermore, a previous experimental study by Elvington et al. has reported a shift in the redox peak potential of the Fe/N/C catalyst from 0.77 V_{RHE} in 0.5 $HClO_4$ to 0.62 V in 0.5 H_2SO_4, assigned to bisulfate adsorption on the catalyst[78]. Based on our calculation results on both FeN4C10 and FeN4CA structure and previous calculations based on FeN_4C_{12} structure[23,24], the anion from the H_2SO_4 solution can thermodynamically adsorb on the FeN_4 site. However, Elvington et al. found no difference in the ORR activity in these two electrolytes, and they have suggested that the bisulfate adsorption does not affect the active site and there is no correlation between the redox potential and the ORR activity for their synthesized Fe/N/C catalyst[78]. It is possible that the adsorption of anions may occur on the sites not involved in the ORR. While various MN_4 structures (e.g., MN_4C_{12}[24,31], MN_4C_{10}[22], MN_4 on zigzag edged[12–14]) have been previously used to study the ligand effect on the ORR activity, the real nature of the sites binding with the anion and the predominated active site in the synthesized sample is still unclear. On top of that, the calculation results obtained for our model might not be general for all types of active sites.

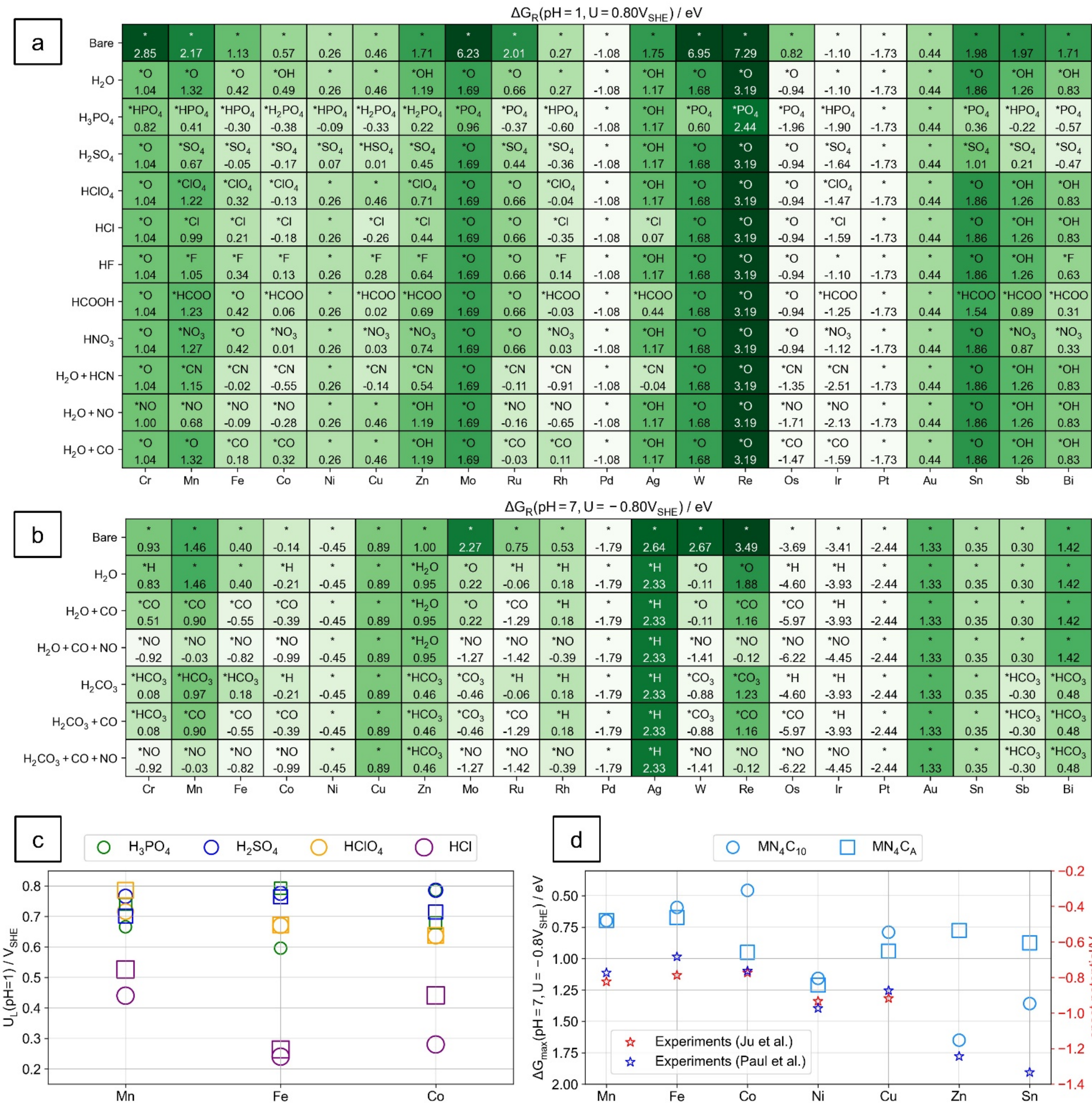

Figure 2 ΔG_R of the most stable adsorbate on MN_4C_{10} in 0.1 M electrolytes at (a) pH = 1, U = 0.80 V_{SHE}. (b) pH = 7, U = -0.80 V_{SHE}. The text insert indicates the most stable adsorbate on the metal site and its corresponding ΔG_R in eV. (c) U_L for the ORR on MN_4C_{10} (circle) and MN_4C_A (square) at pH = 1 with M = Mn, Fe, and Co and (d) ΔG_{max} for the CO_2RR to CO on MN_4C_{10} (circle) and MN_4C_A (square) at pH = 7 and U = -0.8 V_{SHE} with M = Mn, Fe, Co, Ni, Cu, Zn, and Sn.

Evaluating the ORR catalytic activity in 0.5 M H_2SO_4, Martinez *et al.*[13] have reported the following order of onset for the M/N/C catalyst: Mn < Co < Fe and their theoretical study has suggested an *OH ligand as a part of the active site. The theoretical studies by Svane *et al.*[24] based on the MN_4C_{12} structure have reported the same order for the liming potential in 0.5 M H_2SO_4. They have found *HSO_4 as a ligand on the FeN_4C_{12} and MnN_4C_{12} site while *H_2O on the CoN_4C_{12} site in 0.5 M H_2SO_4[24]. According to our calculations, the ligand on MnN_4, FeN_4, and CoN_4 sites on both bulk graphene and graphene edge in 0.1 M H_2SO_4 is *SO_4. As shown in **Figure 2 (c)**, the U_L on the MN_4C_{10} structure for these three elements in 0.1 M H_2SO_4 at pH = 1 differs by 0.01 $V_{SHE,}$ and the U_L order is Mn (0.77 V_{SHE}) < Fe (0.78 V_{SHE}) < Co (0.79 V_{SHE}). While U_L calculated from the MN_4C_A structure in 0.1 M H_2SO_4 is in the following order: Mn (0.70 V_{SHE}) < Co (0.71 V_{SHE}) < Fe (0.76 V_{SHE}), agreeing with the onset potential order from the experiments. Another experimental study testing the ORR performance of the Co/N/C and Mn/N/C catalyst in 0.1 M $HClO_4$ solution has reported the onset potential order as Mn < Co[79]. For both MN_4C_{10} and MN_4C_A sites in 0.1 M $HClO_4$, we find *ClO_4-MnN_4 and *ClO_4-CoN_4 sites serve as the active center, and the U_L is Co < Mn. Based on the MN_4C_{12} structure studied by Svane *et al.*, the ligand is *OH and *H_2O on MnN_4C_{12} and CoN_4C_{12}, respectively, and the U_L is Mn < Co[24].

Consistent with the previous experiments[80], our calculations based on FeN_4C_{10} and FeN_4C_A structures and the FeN_4C_{12} site in the previous computational study[24] suggest a poisoning by CN^- in an acid environment. At U > 0 V_{SHE}, pH = 1, the ORR on the FeN_4C_{10} and FeN_4C_A sites process by the least thermodynamic barrier for removing one *CN anion from the FeN_4 sites. The Fe site and other metal sites such as Mn, Co, Ru, Rh, Os, and Ir on both bulk graphene and graphene edge where two *CN can limit the ORR anions by blocking the metal site at U > 0 V_{SHE}, pH = 1. Additionally, we find that NO gas molecules are thermodynamically favorable on both sides of the IrN_4C_{10} and IrN_4C_A structure. In the potential range of 0 - 0.8 V_{SHE} and pH = 1, the ORR proceeds with the least thermodynamic hindrance for removing one *NO from the IrN_4 site. We find that both CO and NO gas molecules are thermodynamically stable on both sides of the RuN_4C_A and OsN_4C_A structures. However, at U = 0.80 V_{SHE}, pH = 1, the binding of *OH is stronger than the 2^{nd} *CO or *NO. As a result, the ORR is thermodynamically limited by the reduction of *OH to H_2O.

Based on our present calculation results and the previous studies[23,24], it is seen that the nature of the metal center of the M/N/C catalyst and the coordination environment plays a crucial role in determining the electrolyte adsorption and its corresponding catalytic performance in acid environments.

Figures 2 (b) and **S12-S13** show ΔG_R of the most stable MN_4C_{10} and MN_4C_A surface in 0.1 M electrolytes under the CO_2RR condition (pH = 7, and U = -0.8 V_{SHE}). At this condition, we include 0.1 M H_2CO_3 solution as the typical electrolyte used in the experiments[50,53,58]. In contrast to the ORR conditions, the anion from most of the considered electrolytes, except from 0.1 M H_2CO_3, do not bind with the single metal site. Thus, most considered electrolytes possibly have little impact on catalytic activity and stability of the MN_4 site under the CO_2RR. For all considered electrolytes, except 0.1 M H_2CO_3, the stability under the CO_2RR-related condition is the same as in H_2O. We find that *H can occupy the CoN_4, RuN_4, RhN_4, $OsN_{4,}$ and IrN_4 sites on both bulk graphene and the graphene edge in H_2O. While the $MoN_4C_{x=10,A}$, $WN_4C_{x=10,A}$, and ReN_4C_{10} sites are occupied by *O. These results are the same as under the ORR condition but with a lower thermodynamic driving force toward the dissolution. It is also seen that *CO (in H_2O+CO solution) and *NO (in H_2O+CO+NO solution) can be thermodynamically stable on many metal sites both on bulk graphene and the graphene edge. The *NO is likely to bind stronger than *CO to the metal site. The binding of CN^- anion on the metal site is weaker than the CO gas molecule. Then *CN is unlikely to block the metal site or affect the CO_2RR. In 0.1 M H_2CO_3, the $MoN_4C_{x=10,A}$, $WN_4C_{x=10,A}$, and

ReN_4C_{10} sites bind with the $*CO_3$ via two oxygen atoms. For other metal sites, we find that $*HCO_3$ is thermodynamically stable on $CrN_4C_{x=10,A}$, $MnN_4C_{x=10,A}$, FeN_4C_{10}, ZnN_4C_{10}, $SbN_4C_{x=10,A}$, and $BiN_4C_{x=10,A}$ sites. When the CO gas molecule is present (such as in 0.1 M H_2CO_3 + CO), the *CO can compete with $*HCO_3$ and $*CO_3$ and bind to the metal sites. It can be seen that the most stable adsorbate on both MN_4C_{10} and MN_4C_A sites in H_2O+CO and 0.1 M H_2CO_3+CO is slightly different. Similar to the ORR conditions, we found that the NiN4, CuN4, PdN4, PtN4, and AuN4 sites are unoccupied.

Recently, a kinetic model fit the experimental data by Zeng *et al.*[81] demonstrated the role of the bicarbonate (HCO_3) buffer on the electrochemical CO_2RR catalyzed by cobalt phthalocyanine (CoPC). They suggested that the active site can be poisoned by HCO_3^- via electrosorption at low overpotential while the bicarbonate acts as a proton donor at higher overpotential. Defining the onset potential for CO production to be the applied electrode potential at which the TOF of the CO formation exceeds 0.2 mmol/(h m^2_{active}), the experiments have found that the Co/N/C catalyst starts producing CO at around -0.36 V_{RHE}[53] (-0.77 V_{SHE} at pH = 7). Around this potential, it is seen from our calculations in **Figure 1 (c)** and **Figure S6-S7** that *H, *CO, and $*HCO_3$ could be absorbed on the CoN_4 site on both bulk graphene and the graphene edge. At more negative potential (high overpotential), the *H is more stable than *CO and $*HCO_3$. At a more positive potential (low overpotential), the $*HCO_3$ becomes the most favorable adsorbate.

Furthermore, a series of M/N/C catalysts (M = Mn^{3+}, Fe^{3+}, Co^{2+}, Ni^{2+}, Cu^{2+}, Zn^{2+}, and Sn^{2+}) have been synthesized and evaluated for electrochemical CO_2 reduction in aqueous electrolyte (0.5 M $KHCO_3$ and 0.5 M K_2SO_4) by Paul et al.[50]. They have found that the Cu/N/C catalyst can produce hydrocarbon products in significant amounts which have also been demonstrated to correlate with a partial reduction of Cu^{2+} to Cu^0 accompanied by a partial demetallation of the CuN_4 site. According to our calculation at CO_2RR condition in 0.1 M H_2CO_3+CO, both the CuN_4 site and the MnN_4 site on both bulk graphene and the graphene edge have a relatively higher thermodynamic driving force than other metal elements. While our calculation agrees with the experiments for the CuN_4 site by Paul et al.[50], it is inconclusive for the MnN_4 site since there are no available experiments on the transformation of the Mn/N/C catalyst during the CO_2RR.

Similar to the ORR mechanism with the electrolyte anion ligand, the following mechanism for CO_2 to CO formation is considered:

$$*A^n/*A^n + ne^- \rightarrow */*A^n + A^{n-} \quad ; \Delta G(CO_2RR)_0 \qquad \text{Equation 8}$$

$$*/*A^n + CO_2 + (H^+ + e^-) \rightarrow *COOH/*A^n \quad ; \Delta G(CO_2RR)_1 \qquad \text{Equation 9}$$

$$*COOH/*A^n + (H^+ + e^-) \rightarrow *CO/*A^n + H_2O \quad ; \Delta G(CO_2RR)_2 \qquad \text{Equation 10}$$

$$*CO/*A^n \rightarrow CO(g) + */*A^n \quad ; \Delta G(CO_2RR)_3 \qquad \text{Equation 11}$$

The possible electrolyte anion participating in the reaction is considered to be the most stable adsorbate at pH = 7 and U = -0.8 V_{SHE}. The CO_2 to CO formation activity is also considered in this condition. **Figure S21-S22** shows the thermodynamic barrier of the limiting step (ΔG_{max}) for the CO_2 to CO formation at pH = 7 and U = -0.8 V_{SHE} on the MN_4 site. We find that the NO gas molecules thermodynamically prefer both sides of the IrN_4C_{10}, IrN_4C_A, and ReN_4C_A structures. In the H_2CO_3 + CO + NO solution at pH = 7 and U = -0.8 V_{SHE}, the limiting step is removing one NO gas molecule plus forming *COOH on these metal sites. Similarly, the CO gas molecules can be thermodynamically stable on both sites of $ReN_4C_{x=10,A}$, $OsN_4C_{x=10,A}$, RuN_4C_A, and WN_4C_A sites. In H_2CO_3 + CO solution at pH = 7 and U = -

0.8 V_{SHE}, the limiting step on these metal sites is also the removal of one CO gas molecule plus the formation *COOH.

We compare our calculation results with the experimental studies shown in **Figure 2 (d).** An experimental study by Ju et al.[53]. has evaluated the electrochemical performance of the M/N/C catalyst (M=Mn. Fe. Co, Ni, and Cu) for CO_2 to CO formation and reported the order of the onset potential in 0.1 M $KHCO_3$ as follows: Co (-0.36 V_{RHE}) > Fe (-0.37 V_{RHE}) > Mn (-0.41 V_{RHE}) > Cu (-0.52 V_{RHE}) > Ni (-0.36 V_{RHE}). Their theoretical results have also suggested that the potential-determining step on these M/N/C catalysts is the first proton-coupled electron transfer reduction of CO_2 to form *COOH[53]. The experimental onset potentials reported by Ju *et al*. are marked with red stars in **Figure 2 (d)** and use the y-axis on the right. In 0.1 M H_2CO_3 with CO, the CO_2 to CO formation on the MN_4C_{10} structure is thermodynamically limited by the reduction of CO_2 to *COOH, as shown in **Figure S20 (a)**. The thermodynamic barrier of the limiting step for the CO_2 to CO formation at U = -0.80 $V_{SHE,}$ and pH = 7 is found to be in the following order: Co (0.46 eV) < Fe (0.59 eV) < Mn (0.70 eV) < Cu (0.79 eV) < Ni (1.16 eV), agreeing with the onset potential order reported by Ju *et al*.[53]. It should be noted that at this condition in 0.1 M H_2CO_3+CO, the ligand is found to be *CO on the CoN_4C_{10}, $FeN_4C_{10,}$ and MnN_4C_{10} sites. In contrast, the CuN_4C_{10} and NiN_4C_{10} site has no ligand on the metal site at this condition.

For the MN_4C_A structure in 0.1 M H_2CO_3 with CO, the ligand at U = -0.80 $V_{SHE,}$ and pH = 7 is *H on the CoN_4C_A site and *CO on the FeN_4C_A and MnN_4C_A sites. There is also no ligand on both CuN_4C_A and NiN_4C_A under this condition. The CO_2RR to CO reaction on these metal sites is also limited by the reduction of CO_2 to *COOH, as shown in **Figure S20 (b)**, and the thermodynamic barrier of the limiting step at U = -0.80 $V_{SHE,}$ and pH = 7 is in the following order: Fe (0.67 eV) < Mn (0.70 eV) < Cu (0.94 eV) < Co (0.95 eV) < Ni (1.21 eV), deviating from the experimental trend.

Furthermore, Li *et al*.[51] have synthesized and evaluated the activity toward CO formation in 0.1 M $KHCO_3$ for the M/N/C catalysts with M = Mn, Fe, Co, Ni, and Cu. They have reported the following order of CO partial current density at U = -0.6 V_{RHE}: Co > Fe > Ni > Cu > Mn. Our thermodynamic barrier on the MN_4C_{10} structure agrees with this experiment only for the relative order between Co, Fe, and Mn. In another experimental study by Paul *et al*. [50], the M/N/C catalyst with M = Mn, Fe, Co, Ni, Cu, Zn, and Sn was synthesized and tested for the CO_2RR in gas diffusion electrodes. The experimental onset potential for the CO formation in 0.5 M $KHCO_3$+0.5 M K_2SO_4 at pH=7.5 has been reported in the following order: Fe (-0.27 V_{RHE}) > Co (-0.35 V_{RHE}) > Mn (-0.36 V_{RHE}) > Cu (-0.46 V_{RHE}) > Ni (-0.56 V_{RHE}) > Zn (-0.83 V_{RHE}) > Sn (-0.92 V_{RHE}). The experiential onset potentials reported by Paul et al.[50] are marked with blue stars in **Figure 2 (d).** Our thermodynamic barrier based on the MN_4C_{10} and MN_4C_A structure in 0.1 M H_2CO_3 with CO does not give the exact order as the experimental results by Paul et al. [50]

It should be noted that other possible sites with different coordination environments[81–83] could be involved in the catalytic process and that the distribution of active sites could be different in each experiment, depending on the synthesis process. Also, the onset potential is defined differently in these two experiments. Besides, we assume the reaction in the experiments is limited by reducing CO2 to the *COOH step, as our calculations.

On top of that, the most stable ligand could be different when the potential slightly deviates from U = -0.8 V_{SHE} on some metal sites, i.e., the CoN_4C_{10} site. In **Figure S24**, we consider the thermodynamic barrier of the limiting step on the metal site in 0.1 M H_2CO_3+CO at -1.0 V_{SHE} and pH = 7, and the most stable adsorbate at U = -1.0 V_{SHE}, pH = 7 is considered to be a ligand on the metal site. At this condition, most of the considered MN_4C_{10} sites still have the same ligand, except the CoN_4C_{10} site, where the ligand is now *H. For the MN_4C_{10} structure, the limiting step is still the reduction of CO_2 to *COOH step, as shown in **Figure S23(a)**. The thermodynamic barrier of the limiting step at U = -1.0 V_{SHE}, pH = 7 is found in the following order: Fe < Mn < Co < Cu < Ni < Sn < Zn. When the ligand changes, the most active site is shifted from the CoN_4C_{10} site to the FeN_4C_{10} site. Still, this order differs slightly from the experimental trend reported by Paul *et al*. [50]

It should be noted that the oxidation state on the single metal atom in the pristine MN_4 structure is considered to be +2 in this work. Our calculations give a relatively high thermodynamic barrier for the NiN_4 site on both bulk graphene and graphene edge, compared to the FeN_4 site. In contrast, the Fe/N/C and particularly Ni/N/C catalyst have been suggested as highly promising for selective CO production[50,51,53]. One possible explanation is that the $Ni^{2+}N_4$ site is not active for the CO_2RR. According to a previous study by Li *et al*., the $Ni^{1+}N_4C_{10}$ site bind with CO_2 more strongly than the $Ni^{2+}N_4C_{10}$, so the $Ni^{1+}N_4C_{10}$ site is predicted to have higher activity toward CO formation than the $Ni^{2+}N_4C_{10}$ site. In fact, by DFT calculations, they have found that the $Ni^{1+}N_4C_{10}$ site has the highest activity among the considered MN_4 sites in their study where M = Mn^{2+}(*O), Fe^{2+}(*H_2O), Co^{2+}(*H_2O), Ni^{1+}, and Cu^{2+}. The letter in parentheses is the ligand considered in their study[51].

The local environment could also influence catalytic activity. For example, according to a previous study by Yang et al., the NiN_3 sites have been calculated to be more active than the NiN_4 site[84]. Furthermore, it has been suggested that the NiN_y site has a weaker binding of *H than the CoN_y site, making the hydrogen evolution reaction (HER) unfavorable for the Ni/N/C catalyst and the CO selectivity is higher for the Ni/N/C catalyst than the Co/N/C catalyst[53]. As shown in **Figure S25**, the binding energy of *H on the NiN_4 site is weaker than on the CoN_4 site. Thus the NiN_4 site in our calculation is also expected to have higher selectivity toward CO formation than the CoN_4 sites.

Apart from the variations in local carbon structure that possibly result in discrepancies with the experiments, there could be uncertainty associated with the DFT method, i.e., errors in the exchange-correlation functional. A previous theoretical study by Vijay et al. has suggested that the d-state at the Fermi level and binding of CO_2RR intermediate of the FeN_y structure can be well described by HSE06 and GGA+U (a GGA functionals included an appropriate Hubbard-U correction) functional [85]. **Figure S26** compares the stability diagram of the FeN_4C_{10} site in H_2O obtained from a typical GGA level (BEEF-vdW, PBE+D3) and a hybrid functional (HSE06+D3). Our results show that the most stable ligand on the Fe site under the ORR-related condition depends on the exchange-correlation function used in the DFT calculations. Therefore, a careful selection of the exchange-correlation function aligned with the experiments may be needed in order to get a more accurate model. At the same time, hybrid functionals are prohibitively expensive for computational screening in this study.

Additionally, it is important to note that the results obtained for our model are based on the computational hydrogen electrode (CHE) model, assuming zero net charges to simulate a charged surface at the electrochemical interface. The surface charge, in fact, changes along the reaction coordinate at a constant applied potential[86] and many previous studies have shown that a charge fluctuation on the catalyst surface at a constant applied potential is important for describing the binding energy of the ORR and CO_2RR intermediate and the reaction pathways on the catalyst surface[85,87–89]. Therefore, a grand-canonical ensemble of electrons at a chemical potential set by the electrode may better describe the electrochemical interface[86,90–92]. However, grand-canonical DFT calculations are challenging and more computationally demanding, beyond our scope in this study.

Additionally, it should be noted that an explicit solvation model may better describe the effect of solvent interaction, such as hydrogen bonds [93–95]. Dynamically competitive adsorption between water and electrolyte anions may be captured by a fully explicit solvation model with molecular dynamic (MD) simulations. The FeN_4C_{10} sites with H_3PO_4 and H_2PO_4 anions with explicit water molecules are selected to perform the MD simulations. Additional calculation details can be found in section 9 of the supporting information. We found that an H_3PO_4 molecule is not stable on the FeN_4C_{10} site. The $*H_3PO_4$ is likely to desorb and deprotonate, forming $H_2PO_4^-$(aq) + H^+(aq) in the bulk solution, see **Figure S29**. At the same time, the FeN_4C_{10} is likely to be occupied by $*H_2O$. These results align with the thermodynamic calculations with the implicit solvation, as shown in **Figure S31**. Furthermore, we find that the $*H_2PO_4$ is more stable on the FeN_4C_{10} site (in $*H_2PO_4$ + $32H_2O$ system) than $*H_2O$ (in $*H_2PO_4$ + $32H_2O$), suggesting that the $H_2PO_4^{-2}$ may competitively adsorb on the metal site than H_2O (pH ≈ 6-7), see **Figure S30**. Based on our thermodynamic calculation with implicit solvation, we also predict that $*H_2PO_4$ is more stable on the FeN_4C_{10} site than water (at U > 0, pH = 6-8), as shown in **Figure S31(b)**. However, to consider the stability calculations with fully explicit solvation at a wide range of pH and potential, MD simulations with many configurations of water, electrolyte anion, and protons at the interface are required[96,97]. Such calculations are challenging and more computationally expensive beyond the computational screening purpose in this study

In order to identify the promising catalysts that are electrochemically stable and active based on our computational analysis, the ΔG_R of the most stable phase is plotted against its corresponding thermodynamic barrier of the limiting step on that most stable phase at the same condition. We considered the ORR catalyst in acid at U = 0.80 V_{SHE} and pH = 1, as shown in Figures **3 (a)** and **3 (b)**. It is seen that the FeN_4, CoN_4, MnN_4, and RuN_4 sites on both bulk graphene and the graphene edge emerge as promising candidates in many electrolytes, in agreement with several previous experimental studies[2,75,98,99]. In our previous study, where electrolyte adsorption was not included, the MnN_4 and CrN_4 structures were not promising candidates for the ORR in acid condition[18]. The MnN_4 and CrN_4 site, however, becomes more stable against dissolution through electrolyte adsorption in the current study. We also identify new promising combinations between metal elements for acid electrolytes with ΔG_R < 1 eV and ΔG_{max} < 0.8 eV. These are IrN_4C_{10} in H_3PO_4, $HClO_4$, H_2O+NO, or non-adsorbing electrolyte (e.g., HF); IrN_4C_A in H_3PO_4, H_2O+NO or non-adsorbing electrolyte (e.g., $HClO_4$, HF, HCOOH); CuN_4C_A in a non-adsorbing electrolyte (e.g., $HClO_4$, HNO_3); CuN_4C_{10} in H_2SO_4, H_3PO_4, non-adsorbing electrolyte (e.g., $HClO_4$, HNO_3); RhN_4C_{10} in H_2O+CO, $HClO_4$, H_3PO_4, H_2SO_4, H_2O+NO; RhN_4C_A in H_2SO_4, H_2O+NO, H_3PO_4 or non-adsorbing electrolyte (e.g., $HClO_4$, HF, HCOOH); AgN_4C_A in H_3PO_4; $AuN_4C_{x=10,A}$ in a non-adsorbing electrolyte (e.g., all considered electrolytes in this study); ZnN_4C_{10} in $HClO_4$, HNO_3; ZnN_4C_A in $HClO_4$, HNO_3, HCOOH, HCl; OsN_4C_{10} in H_3PO_4 and H_2O+CO; BiN_4C_A in H_3PO_4, $HClO_4$, H_2SO_4, HCOOH; CrN_4C_A in H_2O+NO, H_2SO_4, or non-adsorbing electrolyte (e.g., $HClO_4$, HCl, HCOOH); SnN_4C_A in H_2SO_4, H_3PO_4; and SbN_4C_A in HCOOH, HCl, H_3PO_4. It is seen that the p-block metals, mostly on the graphene edge, have comparable stability and activity to the transition metal sites. The Sn/N/C catalyst has been successfully synthesized, and it exhibits similar activity and selectivity for four-electron ORR to a Fe/N/C catalyst in 0.1 M $HClO_4$[100]. The Sb/N/C catalyst has also been synthesized and exhibits promising activity toward the ORR, although in 0.1 M KOH[101].

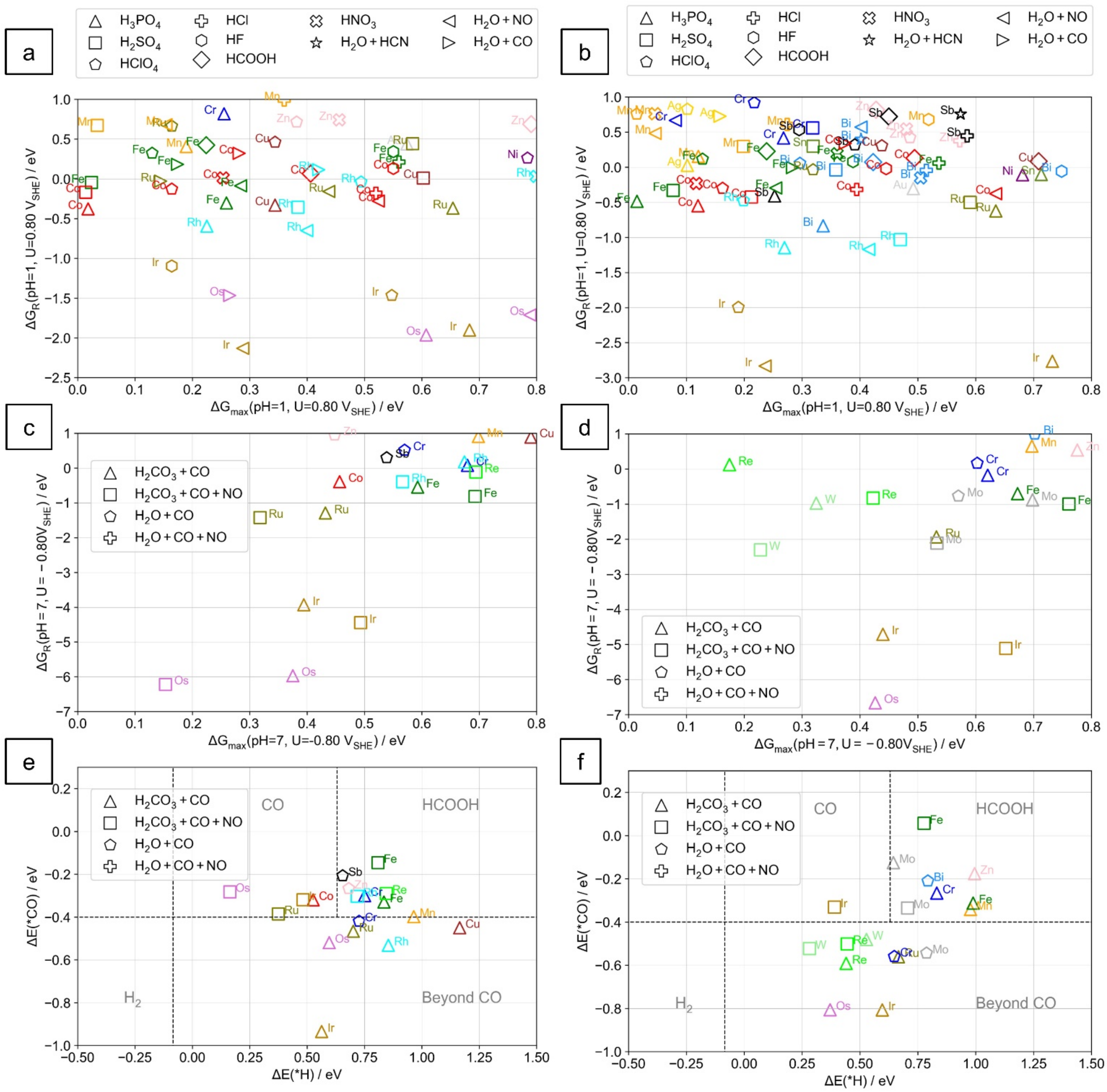

Figure 3 ΔG_R vs. ΔG_{max} for the ORR on the most stable surface in the different electrolytes at pH = 1 at U = 0.8 V_{SHE}: (a) MN_4C_{10} (b) MN_4C_A. ΔG_R vs. ΔG_{max} for the CO_2RR to CO on the most stable surface in different electrolytes at pH = 7 and U = -0.8 V_{SHE}: (c) MN_4C_{10} and (d) MN_4C_A. Classification plot for possible CO_2RR products of promising candidates: (e) MN_4C_{10} and (f) MN_4C_A.

For the CO_2RR toward CO, we consider the condition at U = -0.80 V_{SHE} and pH = 7, as shown in **Figure 3 (c)** and **(d)**. Besides the MnN_4, FeN_4, CoN_4, and NiN_4 which has been experimentally suggested for CO production[50,51,53], we show promising combinations (with ΔG_R < 1 eV and ΔG_{max} < 0.8 eV):

$OsN_4C_{x=10,A}$, $IrN_4C_{x=10,A}$, $RuN_4C_{x=10,A}$, $RhN_4C_{10,}$ FeN_4C_{10}, $ReN_4C_{x=10,A}$, and WN_4C_A in H_2CO_3 (or H_2O) with NO or CO; $BiN_4C_{x=10,A}$ and $SbN_4C_{x=10,A}$ in non-adsorbing electrolyte (e.g. H_2O); ZnN_4C_{10} in H_2O with CO; $CrN_4C_{x=10,A\ in}$ H_2CO_3 with CO, H_2O with CO; MoN_4C_A in H_2CO_3 with CO or NO; and MoN_4C_A in H_2O with CO.

In addition to reducing CO_2 to CO, the competing HER is crucial in determining catalytic efficiency. It has been shown that the binding strength of *CO and *H are a descriptor of CO_2RR selectivity for both on transition metal surface[102] and single site porphyrin-like structure[103]. **Figure 3 (e)** and **(f)** show the classification of possible products from CO_2RR on the single metal sites, based on the binding energy of *CO and *H criteria suggested by Bagger et al.[103]. It is seen that the identified promising candidates are selective toward CO production over H_2 production. The effect of the ligand is seen on the MoN_4, RuN_4, WN_4, ReN_4, and OsN_4 sites, where the bare metal site strongly bonds with *H and will be highly selective for the HER. The binding of *CO and *H becomes weaker with the ligand; thus, the competing HER can be suppressed, as shown in **Figure S25**. Among the promising candidates, $IrN_4C_{x=10,A}$ in H_2CO_3 with CO, and OsN_4C_A in H_2CO_3+CO solution potentially reduces CO_2 to the product beyond CO. Other promising candidates that can produce products beyond CO are $RuN_4C_{x=10,A}$, $RhN_4C_{10,}$ and OsN_4C_{10} in H_2CO_3+CO solution; ReN_4C_A and WN_4C_A in H_2CO_3+CO (or H_2CO_3+CO+NO solution); and CrN_4C_A and MoN_4C_A in H_2O+CO solution.

For the transition metal single atom considered in this study, we find that the reaction intermediate binding on the MN_4 site on the graphene edge is generally weaker than that on the MN_4 site on the bulk graphene. **Figure S32** illustrates the projected density of states (PDOS) for the CoN_4C_{10} and CoN_4C_A sites without and with adsorbate (either one *OH or *COOH adsorbate). In the pristine structure of the CoN_4C_{10} site, we observe that the $3d_{xy}$ hybridization with the 2p orbital of the surrounding N atoms forms the Co-N bonds, while the other 3d orbitals are non-binding orbitals. For the pristine structure of the CoN_4C_A site, not only $3d_{xy}$ but also $3d_{x2-y2}$ overlap with the 2p orbital for the surrounding N atoms. When *OH or *COOH adsorb on the Co atom, the 2p orbital of *OH or *COOH overlaps with the $3d_{z2}$ and $3d_{yz}$ orbital of the Co atom for the CoN_4C_{10} and CoN_4C_A site. In the CoN_4C_{10} site, the Co $3d_{x2}$ orbital locates below, while the Co $3d_{xy}$ locates above the Fermi energy. The opposite situation is found for the CoN_4C_A site, where the Co $3d_{x2}$ orbital locates below while the Co $3d_{xy}$ locates above the Fermi energy. A similar calculated PDOS pattern is found for other single metal atoms. Thus, it appears that the difference in d-orbitals located near the Fermi level, possibly caused by different local carbon atoms, affects the binding strength of the adsorbates[7].

Furthermore, with the presence of the ligand on the other side of the single metal atom, we find that the adsorption of the reaction intermediate likely weakens. The change in adsorption behavior of the ORR intermediate with the ligand on the CrN_4C_{12} and the CoN_4C_{12} structure has been previously explained by Svane et al. [24,31] using crystal field theory. In **Figure S33**, we show the possible electronic configuration in the d-orbital of the single metal atom in the MN_4C_{10} (M = Cr, Mn, Fe, and Co) structure with one and two adsorbates based on the converged magnetization and crystal field theory. The MN_4 site with two adsorbates adopts an octahedral structure, and the d-orbitals of the metal atom are split into two different energy levels, t_{2g} and e_g. For a Co^{2+} ion with a low spin configuration in the octahedral geometry, transferring more than one electron to the adsorbates may not be thermodynamically favorable since after the first unpaired electron is transferred from higher e_g d-orbitals, the remaining electrons are paired electrons and entirely placed in the lower t_{2g} d-orbital.

Similarly, for a Fe^{2+} ion in the octahedral geometry with a low spin configuration, all d-electrons are placed in the lower t_{2g} d-orbital. Removing electrons from this fully occupied orbital may not be thermodynamically favorable. This could result in the destabilization of *COOH or *OH when binding as the second adsorbate. We find a similar value of the final magnetization for the MN_4 site on both bulk graphene and graphene edge; thus, we expect that both structure sites should have a similar d-orbital splitting pattern.

CONCLUSION

We have investigated the effect of electrolyte anion adsorption on the stability and activity of single metal atoms doped on two different graphenes: the bulk graphene terrace and a graphene edge with 3d, 4d, 5d, or p-block (Sn, Sb, and Bi) metal atoms. We find that the armchair edge is thermodynamically favored to form the MN_4 site compared to the bulk graphene, especially for 3d transition metals. Under ORR conditions (pH=1 and U=0.80 V_{SHE}), we find that various electrolyte anions can compete with water and adsorb on the single metal site. The electrolyte anion adsorption depends on the nature of the metal atom and local carbon around the MN_4 site. The ORR activity is either poisoned or altered by the electrolyte anion. If the electrolyte anion adsorbs on the single metal site, the single metal site can be further stabilized against dissolution in acid environments, compared to the stability in the pure water environment. We also find that the MN_4 site on the armchair edge is more stable than on the bulk graphene. Therefore, it would be interesting to include the electrolyte stabilization effect on other MN_4 sites with different local carbon structures, although the sites considered here are expected to be among the most stable sites. Considering both stability in acid conditions and ORR activity, we find a single metal site based on Ir, Cu, Rh, Zn, Au, Os, Cr, and p-block elements (Sb, Sn, and Bi), especially on the graphene edge, has comparable ORR activity and stability to a single metal atom based on Fe and Co. Under the CO_2RR condition (pH = 7 and U = -0.8 V_{SHE}), most considered electrolyte anions, except in 0.1 M H_2CO_3 solution, do not interact with the single metal site. Still, water and gas molecules may form ligands on various single metal sites under CO_2RR conditions. We find that the activity trend for reducing CO_2 to CO on the single metal site with the ligand from the solution compares well with the experimental trends. Besides the single atom catalyst-based Fe, Co, and Ni, we have identified promising single metal sites (Cr, Ru, W, Re, Os, Rh, Bi, Sb, Mo, Zn, and Ir) by including the adsorbate ligand from the solution. These promising candidates have comparable stability and activity to the Fe and Co-based catalysts. Our results illustrate that the nature of the metal atom, the local carbon structure, and the chemical environment, such as electrolytes, play a critical role in the activity and stability of a single-atom electrocatalyst. A careful combination of electrolyte or gas ligand and a single metal atom with various local carbon could be a possible way to achieve an active and durable electrocatalyst.

DATA AVAILABILITY

The data that supports the findings of this study are available within the article and its supplementary material. The DFT-optimized structures and calculation details in this study can be accessed from an online repository: DOI:10.5281/zenodo.7071450

SUPPLEMENTARY MATERIAL

See supplementary material for complete computational details and supporting results in figure S1-S33 and table S1-S4.

ACKNOWLEDGMENTS

Funding from the Villum Foundation V-SUSTAIN grant 9455 to the Villum Center for the Science of Sustainable Fuels and Chemicals and a scholarship from the Ministry of Science and Technology, Royal Thai Government is acknowledged.

REFERENCE

(1) He, Y.; Shi, Q.; Shan, W.; Li, X.; Kropf, A. J.; Wegener, E. C.; Wright, J.; Karakalos, S.; Su, D.; Cullen, D. A.; Wang, G.; Myers, D. J.; Wu, G. Dynamically Unveiling Metal–Nitrogen Coordination during Thermal Activation to Design High-Efficient Atomically Dispersed CoN4 Active Sites. *Angewandte Chemie - International Edition* **2021**, *60* (17), 9516–9526. https://doi.org/10.1002/anie.202017288.

(2) Zitolo, A.; Ranjbar-Sahraie, N.; Mineva, T.; Li, J.; Jia, Q.; Stamatin, S.; Harrington, G. F.; Lyth, S. M.; Krtil, P.; Mukerjee, S.; Fonda, E.; Jaouen, F. Identification of Catalytic Sites in Cobalt-Nitrogen-Carbon Materials for the Oxygen Reduction Reaction. *Nat Commun* **2017**, *8* (1), 957. https://doi.org/10.1038/s41467-017-01100-7.

(3) Lefèvre, M.; Proietti, E.; Jaouen, F.; Dodelet, J. P. Iron-Based Catalysts with Improved Oxygen Reduction Activity in Polymer Electrolyte Fuel Cells. *Science (1979)* **2009**, *324* (5923), 71–74. https://doi.org/10.1126/science.1170051.

(4) Zitolo, A.; Goellner, V.; Armel, V.; Sougrati, M. T.; Mineva, T.; Stievano, L.; Fonda, E.; Jaouen, F. Identification of Catalytic Sites for Oxygen Reduction in Iron- and Nitrogen-Doped Graphene Materials. *Nat Mater* **2015**, *14* (9), 937–942. https://doi.org/10.1038/nmat4367.

(5) Zhang, H.; Chung, H. T.; Cullen, D. A.; Wagner, S.; Kramm, U. I.; More, K. L.; Zelenay, P.; Wu, G. High-Performance Fuel Cell Cathodes Exclusively Containing Atomically Dispersed Iron Active Sites. *Energy Environ Sci* **2019**, *12* (8), 2548–2558. https://doi.org/10.1039/c9ee00877b.

(6) Varela, A. S.; Ranjbar Sahraie, N.; Steinberg, J.; Ju, W.; Oh, H.-S.; Strasser, P. Metal-Doped Nitrogenated Carbon as an Efficient Catalyst for Direct CO 2 Electroreduction to CO and Hydrocarbons . *Angewandte Chemie* **2015**, *127* (37), 10908–10912. https://doi.org/10.1002/ange.201502099.

(7) Liu, K.; Wu, G.; Wang, G. Role of Local Carbon Structure Surrounding FeN4 Sites in Boosting the Catalytic Activity for Oxygen Reduction. *Journal of Physical Chemistry C* **2017**, *121* (21), 11319–11324. https://doi.org/10.1021/acs.jpcc.7b00913.

(8) Li, J.; Sougrati, M. T.; Zitolo, A.; Ablett, J. M.; Oğuz, I. C.; Mineva, T.; Matanovic, I.; Atanassov, P.; Huang, Y.; Zenyuk, I.; di Cicco, A.; Kumar, K.; Dubau, L.; Maillard, F.; Dražić, G.; Jaouen, F. Identification of Durable and Non-Durable FeNx Sites in Fe–N–C Materials for Proton Exchange Membrane Fuel Cells. *Nat Catal* **2021**, *4* (1), 10–19. https://doi.org/10.1038/s41929-020-00545-2.

(9) Charreteur, F.; Jaouen, F.; Ruggeri, S.; Dodelet, J. P. Fe/N/C Non-Precious Catalysts for PEM Fuel Cells: Influence of the Structural Parameters of Pristine Commercial Carbon Blacks on Their Activity for Oxygen Reduction. *Electrochim Acta* **2008**, *53* (6), 2925–2938. https://doi.org/10.1016/j.electacta.2007.11.002.

(10) Qin, X.; Zhu, S.; Xiao, F.; Zhang, L.; Shao, M. Active Sites on Heterogeneous Single-Iron-Atom Electrocatalysts in CO2 Reduction Reaction. *ACS Energy Lett* **2019**, *4* (7), 1778–1783. https://doi.org/10.1021/acsenergylett.9b01015.

(11) Mineva, T.; Matanovic, I.; Atanassov, P.; Sougrati, M. T.; Stievano, L.; Clémancey, M.; Kochem, A.; Latour, J. M.; Jaouen, F. Understanding Active Sites in Pyrolyzed Fe-N-C Catalysts for Fuel Cell Cathodes by Bridging Density Functional Theory Calculations and 57Fe Mössbauer Spectroscopy. *ACS Catal* **2019**, *9* (10), 9359–9371. https://doi.org/10.1021/acscatal.9b02586.

(12) Holby, E. F.; Wu, G.; Zelenay, P.; Taylor, C. D. Structure of Fe-Nx-C Defects in Oxygen Reduction Reaction Catalysts from First-Principles Modeling. *Journal of Physical Chemistry C* **2014**, *118* (26), 14388–14393. https://doi.org/10.1021/jp503266h.

(13) Martinez, U.; Holby, E. F.; Babu, S. K.; Artyushkova, K.; Lin, L.; Choudhury, S.; Purdy, G. M.; Zelenay, P. Experimental and Theoretical Trends of PGM-Free Electrocatalysts for the Oxygen Reduction Reaction with Different Transition Metals. *J Electrochem Soc* **2019**, *166* (7), F3136–F3142. https://doi.org/10.1149/2.0201907jes.

(14) Chung, H. T.; Cullen, D. A.; Higgins, D.; Sneed, B. T.; Holby, E. F.; More, K. L.; Zelenay, P. Direct Atomic-Level Insight into the Active Sites of a High-Performance PGM-Free ORR Catalyst. *Science (1979)* **2017**, *357* (6350), 479–484. https://doi.org/10.1126/science.aan2255.

(15) Kumar, K.; Gairola, P.; Lions, M.; Ranjbar-Sahraie, N.; Mermoux, M.; Dubau, L.; Zitolo, A.; Jaouen, F.; Maillard, F. Physical and Chemical Considerations for Improving Catalytic Activity and Stability of Non-Precious-Metal Oxygen Reduction Reaction Catalysts. *ACS Catal* **2018**, *8* (12), 11264–11276. https://doi.org/10.1021/acscatal.8b02934.

(16) Glibin, V.; Zhang, G.; Dodelet, J.-P.; Sun, S. Non-PGM Electrocatalysts for PEM Fuel Cells: Thermodynamic Stability of Potential ORR CoNx-C Electrocatalytic Sites. *J Electrochem Soc* **2021**, *168* (9), 094502. https://doi.org/10.1149/1945-7111/ac1d03.

(17) Glibin, V. P.; Dodelet, J.-P. Thermodynamic Stability in Acid Media of FeN 4 -Based Catalytic Sites Used for the Reaction of Oxygen Reduction in PEM Fuel Cells . *J Electrochem Soc* **2017**, *164* (9), F948–F957. https://doi.org/10.1149/2.1041709jes.

(18) Hansen, H. A.; Patniboon, T. Acid-Stable and Active M−N−C Catalysts for the Oxygen Reduction Reaction: The Role of Local Structure. *ACS Catal* **2021**, *11* (21), 13102–13118. https://doi.org/10.1021/acscatal.1c02941.

(19) Holby, E. F.; Wang, G.; Zelenay, P. Acid Stability and Demetalation of PGM-Free ORR Electrocatalyst Structures from Density Functional Theory: A Model for "Single-Atom Catalyst" Dissolution. *ACS Catal* **2020**, *10* (24), 14527–14539. https://doi.org/10.1021/acscatal.0c02856.

(20) Nematollahi, P.; Barbiellini, B.; Bansil, A.; Lamoen, D.; Qingying, J.; Mukerjee, S.; Neyts, E. C. Identification of a Robust and Durable FeN 4 C x Catalyst for ORR in PEM Fuel Cells and the Role of the Fifth Ligand . *ACS Catal* **2022**, 7541–7549. https://doi.org/10.1021/acscatal.2c01294.

(21) Xu, X.; Zhang, X.; Kuang, Z.; Xia, Z.; Rykov, A. I.; Yu, S.; Wang, J.; Wang, S.; Sun, G. Investigation on the Demetallation of Fe-N-C for Oxygen Reduction Reaction: The Influence of Structure and Structural Evolution of Active Site. *Appl Catal B* **2022**, *309*. https://doi.org/10.1016/j.apcatb.2022.121290.

(22) Holst-Olesen, K.; Silvioli, L.; Rossmeisl, J.; Arenz, M. Enhanced Oxygen Reduction Reaction on Fe/N/C Catalyst in Acetate Buffer Electrolyte. *ACS Catal* **2019**, *9* (4), 3082–3089. https://doi.org/10.1021/acscatal.8b04609.

(23) Holst-Olesen, K.; Reda, M.; Hansen, H. A.; Vegge, T.; Arenz, M. Enhanced Oxygen Reduction Activity by Selective Anion Adsorption on Non-Precious-Metal Catalysts. *ACS Catal* **2018**, *8* (8), 7104–7112. https://doi.org/10.1021/acscatal.8b01584.

(24) Svane, K. L.; Reda, M.; Vegge, T.; Hansen, H. A. Improving the Activity of M−N4 Catalysts for the Oxygen Reduction Reaction by Electrolyte Adsorption. *ChemSusChem* **2019**, *12* (23), 5133–5141. https://doi.org/10.1002/cssc.201902443.

(25) Zhang, B.; Zhang, J.; Shi, J.; Tan, D.; Liu, L.; Zhang, F.; Lu, C.; Su, Z.; Tan, X.; Cheng, X.; Han, B.; Zheng, L.; Zhang, J. Manganese Acting as a High-Performance Heterogeneous Electrocatalyst in Carbon Dioxide Reduction. *Nat Commun* **2019**, *10* (1). https://doi.org/10.1038/s41467-019-10854-1.

(26) Jia, Q.; Ramaswamy, N.; Hafiz, H.; Tylus, U.; Strickland, K.; Wu, G.; Barbiellini, B.; Bansil, A.; Holby, E. F.; Zelenay, P.; Mukerjee, S. Experimental Observation of Redox-Induced Fe-N Switching Behavior as a Determinant Role for Oxygen Reduction Activity. *ACS Nano* **2015**, *9* (12), 12496–12505. https://doi.org/10.1021/acsnano.5b05984.

(27) Holby, E. F.; Taylor, C. D. Activity of N-Coordinated Multi-Metal-Atom Active Site Structures for Pt-Free Oxygen Reduction Reaction Catalysis: Role of ∗OH Ligands. *Sci Rep* **2015**, *5*. https://doi.org/10.1038/srep09286.

(28) Anderson, A. B.; Holby, E. F. Pathways for O2 Electroreduction over Substitutional FeN4, HOFeN4, and OFeN4 in Graphene Bulk Sites: Critical Evaluation of Overpotential Predictions Using LGER and CHE Models. *Journal of Physical Chemistry C* **2019**, *123* (30), 18398–18409. https://doi.org/10.1021/acs.jpcc.9b03703.

(29) Szakacs, C. E.; Lefèvre, M.; Kramm, U. I.; Dodelet, J. P.; Vidal, F. A Density Functional Theory Study of Catalytic Sites for Oxygen Reduction in Fe/N/C Catalysts Used in H2/O2 Fuel Cells. *Physical Chemistry Chemical Physics* **2014**, *16* (27), 13654–13661. https://doi.org/10.1039/c3cp55331k.

(30) Busch, M.; Halck, N. B.; Kramm, U. I.; Siahrostami, S.; Krtil, P.; Rossmeisl, J. Beyond the Top of the Volcano? – A Unified Approach to Electrocatalytic Oxygen Reduction and Oxygen Evolution. *Nano Energy* **2016**, *29*, 126–135. https://doi.org/10.1016/j.nanoen.2016.04.011.

(31) Svane, K. L.; Hansen, H. A.; Vegge, T. A Comparison of Single and Double Co Sites Incorporated in N-Doped Graphene for the Oxygen Reduction Reaction. *J Catal* **2021**, *393*, 230–237. https://doi.org/https://doi.org/10.1016/j.jcat.2020.11.024.

(32) Yang, X.; Xia, D.; Kang, Y.; Du, H.; Kang, F.; Gan, L.; Li, J. Unveiling the Axial Hydroxyl Ligand on Fe-N4-C Electrocatalysts and Its Impact on the PH-Dependent Oxygen Reduction Activities and Poisoning Kinetics. *Advanced Science* **2020**, *7* (12), 1–6. https://doi.org/10.1002/advs.202000176.

(33) Wang, Y.; Yuan, H.; Li, Y.; Chen, Z. Two-Dimensional Iron-Phthalocyanine (Fe-Pc) Monolayer as a Promising Single-Atom-Catalyst for Oxygen Reduction Reaction: A Computational Study. *Nanoscale* **2015**, *7* (27), 11633–11641. https://doi.org/10.1039/c5nr00302d.

(34) Wagner, S.; Martinaiou, I.; Shahraei, A.; Weidler, N.; Kramm, U. I. On the Effect of Sulfite Ions on the Structural Composition and ORR Activity of Fe-N-C Catalysts. *Hyperfine Interact* **2018**, *239* (1). https://doi.org/10.1007/s10751-017-1485-8.

(35) Wang, F.; Zhou, Y.; Lin, S.; Yang, L.; Hu, Z.; Xie, D. Axial Ligand Effect on the Stability of Fe–N–C Electrocatalysts for Acidic Oxygen Reduction Reaction. *Nano Energy* **2020**, *78*. https://doi.org/10.1016/j.nanoen.2020.105128.

(36) Han, Y.; Wang, Y.; Xu, R.; Chen, W.; Zheng, L.; Han, A.; Zhu, Y.; Zhang, J.; Zhang, H.; Luo, J.; Chen, C.; Peng, Q.; Wang, D.; Li, Y. Electronic Structure Engineering to Boost Oxygen Reduction Activity by Controlling the Coordination of the Central Metal. *Energy Environ Sci* **2018**, *11* (9), 2348–2352. https://doi.org/10.1039/c8ee01481g.

(37) Xiao, M.; Zhang, H.; Chen, Y.; Zhu, J.; Gao, L.; Jin, Z.; Ge, J.; Jiang, Z.; Chen, S.; Liu, C.; Xing, W. Identification of Binuclear Co2N5 Active Sites for Oxygen Reduction Reaction with More than One Magnitude Higher Activity than Single Atom CoN4 Site. *Nano Energy* **2018**, *46*, 396–403. https://doi.org/10.1016/j.nanoen.2018.02.025.

(38) Zhu, Y.; Zhang, B.; Liu, X.; Wang, D. W.; Su, D. S. Unravelling the Structure of Electrocatalytically Active Fe-n Complexes in Carbon for the Oxygen Reduction Reaction. *Angewandte Chemie - International Edition* **2014**, *53* (40), 10673–10677. https://doi.org/10.1002/anie.201405314.

(39) Wei, P. J.; Yu, G. Q.; Naruta, Y.; Liu, J. G. Covalent Grafting of Carbon Nanotubes with a Biomimetic Heme Model Compound to Enhance Oxygen Reduction Reactions. *Angewandte Chemie - International Edition* **2014**, *53* (26), 6659–6663. https://doi.org/10.1002/anie.201403133.

(40) Chen, Z.; Huang, A.; Yu, K.; Cui, T.; Zhuang, Z.; Liu, S.; Li, J.; Tu, R.; Sun, K.; Tan, X.; Zhang, J.; Liu, D.; Zhang, Y.; Jiang, P.; Pan, Y.; Chen, C.; Peng, Q.; Li, Y. Fe1N4-O1site with Axial Fe-O Coordination for Highly Selective CO2reduction over a Wide Potential Range. *Energy Environ Sci* **2021**, *14* (6), 3430–3437. https://doi.org/10.1039/d1ee00569c.

(41) Wang, X.; Wang, Y.; Sang, X.; Zheng, W.; Zhang, S.; Shuai, L.; Yang, B.; Li, Z.; Chen, J.; Lei, L.; Adli, N. M.; Leung, M. K. H.; Qiu, M.; Wu, G.; Hou, Y. Dynamic Activation of Adsorbed Intermediates via Axial Traction for the Promoted Electrochemical CO2 Reduction. *Angewandte Chemie - International Edition* **2021**, *60* (8), 4192–4198. https://doi.org/10.1002/anie.202013427.

(42) Glibin, V. P.; Cherif, M.; Vidal, F.; Dodelet, J.-P.; Zhang, G.; Sun, S. Non-PGM Electrocatalysts for PEM Fuel Cells: Thermodynamic Stability and DFT Evaluation of Fluorinated FeN 4 -Based ORR Catalysts . *J Electrochem Soc* **2019**, *166* (7), F3277–F3286. https://doi.org/10.1149/2.0341907jes.

(43) Wei, J.; Xia, D.; Wei, Y.; Zhu, X.; Li, J.; Gan, L. Probing the Oxygen Reduction Reaction Intermediates and Dynamic Active Site Structures of Molecular and Pyrolyzed Fe–N–C Electrocatalysts by In Situ Raman Spectroscopy. *ACS Catal* **2022**, 7811–7820. https://doi.org/10.1021/acscatal.2c00771.

(44) Sun, F.; Li, F.; Tang, Q. Spin State as a Participator for Demetalation Durability and Activity of Fe–N–C Electrocatalysts. *The Journal of Physical Chemistry C* **2022**. https://doi.org/10.1021/acs.jpcc.2c03518.

(45) Zheng, F.; Ji, Y.; Dong, H.; Liu, C.; Chen, S.; Li, Y. Edge Effect Promotes Graphene-Confining Single-Atom Co–N4 and Rh–N4 for Bifunctional Oxygen Electrocatalysis. *Journal of Physical Chemistry C* **2022**, *126* (1), 30–39. https://doi.org/10.1021/acs.jpcc.1c07691.

(46) Cometto, C.; Ugolotti, A.; Grazietti, E.; Moretto, A.; Bottaro, G.; Armelao, L.; di Valentin, C.; Calvillo, L.; Granozzi, G. Copper Single-Atoms Embedded in 2D Graphitic Carbon Nitride for the CO2 Reduction. *NPJ 2D Mater Appl* **2021**, *5* (1). https://doi.org/10.1038/s41699-021-00243-y.

(47) Byon, H. R.; Suntivich, J.; Shao-Horn, Y. Graphene-Based Non-Noble-Metal Catalysts for Oxygen Reduction Reaction in Acid. *Chemistry of Materials* **2011**, *23* (15), 3421–3428. https://doi.org/10.1021/cm2000649.

(48) He, J.; Zheng, T.; Wu, D.; Zhang, S.; Gu, M.; He, Q. Insights into the Determining Effect of Carbon Support Properties on Anchoring Active Sites in Fe-N-C Catalysts toward the Oxygen Reduction Reaction. *ACS Catal* **2022**, *12* (3), 1601–1613. https://doi.org/10.1021/acscatal.1c04815.

(49) Xiao, M.; Zhu, J.; Ma, L.; Jin, Z.; Ge, J.; Deng, X.; Hou, Y.; He, Q.; Li, J.; Jia, Q.; Mukerjee, S.; Yang, R.; Jiang, Z.; Su, D.; Liu, C.; Xing, W. Microporous Framework Induced Synthesis of Single-Atom Dispersed Fe-N-C Acidic ORR Catalyst and Its in Situ Reduced Fe-N4 Active Site Identification Revealed by X-Ray Absorption Spectroscopy. *ACS Catalysis*. American Chemical Society April 6, 2018, pp 2824–2832. https://doi.org/10.1021/acscatal.8b00138.

(50) Paul, S.; Kao, Y. L.; Ni, L.; Ehnert, R.; Herrmann-Geppert, I.; van de Krol, R.; Stark, R. W.; Jaegermann, W.; Kramm, U. I.; Bogdanoff, P. Influence of the Metal Center in M−N−C Catalysts on the CO2 Reduction Reaction on Gas Diffusion Electrodes. *ACS Catal* **2021**, *11* (9), 5850–5864. https://doi.org/10.1021/acscatal.0c05596.

(51) Li, J.; Pršlja, P.; Shinagawa, T.; Martín Fernández, A. J.; Krumeich, F.; Artyushkova, K.; Atanassov, P.; Zitolo, A.; Zhou, Y.; García-Muelas, R.; López, N.; Pérez-Ramírez, J.; Jaouen, F. Volcano Trend in Electrocatalytic Co2 Reduction Activity over Atomically Dispersed Metal Sites on Nitrogen-Doped Carbon. *ACS Catal* **2019**, *9* (11), 10426–10439. https://doi.org/10.1021/acscatal.9b02594.

(52) Santori, P. G.; Speck, F. D.; Li, J.; Zitolo, A.; Jia, Q.; Mukerjee, S.; Cherevko, S.; Jaouen, F. Effect of Pyrolysis Atmosphere and Electrolyte PH on the Oxygen Reduction Activity, Stability and Spectroscopic Signature of FeN x Moieties in Fe-N-C Catalysts . *J Electrochem Soc* **2019**, *166* (7), F3311–F3320. https://doi.org/10.1149/2.0371907jes.

(53) Ju, W.; Bagger, A.; Hao, G. P.; Varela, A. S.; Sinev, I.; Bon, V.; Roldan Cuenya, B.; Kaskel, S.; Rossmeisl, J.; Strasser, P. Understanding Activity and Selectivity of Metal-Nitrogen-Doped Carbon Catalysts for Electrochemical Reduction of CO2. *Nat Commun* **2017**, *8* (1). https://doi.org/10.1038/s41467-017-01035-z.

(54) Jiang, R.; Li, L.; Sheng, T.; Hu, G.; Chen, Y.; Wang, L. Edge-Site Engineering of Atomically Dispersed Fe-N4 by Selective C-N Bond Cleavage for Enhanced Oxygen Reduction Reaction Activities. *J Am Chem Soc* **2018**, *140* (37), 11594–11598. https://doi.org/10.1021/jacs.8b07294.

(55) Holby, E. F.; Zelenay, P. Linking Structure to Function: The Search for Active Sites in Non-Platinum Group Metal Oxygen Reduction Reaction Catalysts. *Nano Energy* **2016**, *29*, 54–64. https://doi.org/10.1016/j.nanoen.2016.05.025.

(56) Zamora Zeledón, J. A.; Kamat, G. A.; Gunasooriya, G. T. K. K.; Nørskov, J. K.; Stevens, M. B.; Jaramillo, T. F. Probing the Effects of Acid Electrolyte Anions on Electrocatalyst Activity and Selectivity for the Oxygen Reduction Reaction. *ChemElectroChem* **2021**, *8* (13), 2467–2478. https://doi.org/10.1002/celc.202100500.

(57) Kamat, G. A.; Zamora Zeledón, J. A.; Gunasooriya, G. T. K. K.; Dull, S. M.; Perryman, J. T.; Nørskov, J. K.; Stevens, M. B.; Jaramillo, T. F. Acid Anion Electrolyte Effects on Platinum for Oxygen and Hydrogen Electrocatalysis. *Commun Chem* **2022**, *5* (1). https://doi.org/10.1038/s42004-022-00635-1.

(58) Varela, A. S.; Kroschel, M.; Leonard, N. D.; Ju, W.; Steinberg, J.; Bagger, A.; Rossmeisl, J.; Strasser, P. PH Effects on the Selectivity of the Electrocatalytic CO2 Reduction on Graphene-Embedded Fe-N-C Motifs: Bridging Concepts between Molecular Homogeneous and Solid-State Heterogeneous Catalysis. *ACS Energy Lett* **2018**, *3* (4), 812–817. https://doi.org/10.1021/acsenergylett.8b00273.

(59) Kneebone, J. L.; Daifuku, S. L.; Kehl, J. A.; Wu, G.; Chung, H. T.; Hu, M. Y.; Alp, E. E.; More, K. L.; Zelenay, P.; Holby, E. F.; Neidig, M. L. A Combined Probe-Molecule, Mössbauer, Nuclear Resonance Vibrational Spectroscopy, and Density Functional Theory Approach for Evaluation of Potential Iron Active Sites in an Oxygen Reduction Reaction Catalyst. *Journal of Physical Chemistry C* **2017**, *121* (30), 16283–16290. https://doi.org/10.1021/acs.jpcc.7b03779.

(60) Zhang, Q.; Mamtani, K.; Jain, D.; Ozkan, U.; Asthagiri, A. CO Poisoning Effects on FeNC and CNx ORR Catalysts: A Combined Experimental-Computational Study. *Journal of Physical Chemistry C* **2016**, *120* (28), 15173–15184. https://doi.org/10.1021/acs.jpcc.6b03933.

(61) Cho, M.; Song, J. T.; Back, S.; Jung, Y.; Oh, J. The Role of Adsorbed CN and Cl on an Au Electrode for Electrochemical CO2 Reduction. *ACS Catal* **2018**, *8* (2), 1178–1185. https://doi.org/10.1021/acscatal.7b03449.

(62) Malko, D.; Kucernak, A.; Lopes, T. In Situ Electrochemical Quantification of Active Sites in Fe-N/C Non-Precious Metal Catalysts. *Nat Commun* **2016**, *7*. https://doi.org/10.1038/ncomms13285.

(63) Malko, D.; Kucernak, A.; Lopes, T. Performance of Fe-N/C Oxygen Reduction Electrocatalysts toward NO2-, NO, and NH2OH Electroreduction: From Fundamental Insights into the Active Center to a New Method for Environmental Nitrite Destruction. *J Am Chem Soc* **2016**, *138* (49), 16056–16068. https://doi.org/10.1021/jacs.6b09622.

(64) Boldrin, P.; Malko, D.; Mehmood, A.; Kramm, U. I.; Wagner, S.; Paul, S.; Weidler, N.; Kucernak, A. Deactivation, Reactivation and Super-Activation of Fe-N/C Oxygen Reduction Electrocatalysts: Gas Sorption, Physical and Electrochemical Investigation Using NO and O2. *Appl Catal B* **2021**, *292*. https://doi.org/10.1016/j.apcatb.2021.120169.

(65) Sahraie, N. R.; Kramm, U. I.; Steinberg, J.; Zhang, Y.; Thomas, A.; Reier, T.; Paraknowitsch, J.-P.; Strasser, P. Quantifying the Density and Utilization of Active Sites in Non-Precious Metal Oxygen Electroreduction Catalysts. *Nat Commun* **2015**, *6*, 8618. https://doi.org/10.1038/ncomms9618.

(66) Nørskov, J. K.; Rossmeisl, J.; Logadottir, A.; Lindqvist, L.; Kitchin, J. R.; Bligaard, T.; Jónsson, H. Origin of the Overpotential for Oxygen Reduction at a Fuel-Cell Cathode. *Journal of Physical Chemistry B* **2004**, *108* (46), 17886–17892. https://doi.org/10.1021/jp047349j.

(67) Chen, Z.; Jiang, S.; Kang, G.; Nguyen, D.; Schatz, G. C.; van Duyne, R. P. Operando Characterization of Iron Phthalocyanine Deactivation during Oxygen Reduction Reaction Using Electrochemical Tip-Enhanced Raman Spectroscopy. *J Am Chem Soc* **2019**, *141* (39), 15684–15692. https://doi.org/10.1021/jacs.9b07979.

(68) Choi, C. H.; Baldizzone, C.; Grote, J.-P.; Schuppert, A. K.; Jaouen, F.; Mayrhofer, K. J. J. Stability of Fe-N-C Catalysts in Acidic Medium Studied by Operando Spectroscopy. *Angewandte Chemie* **2015**, *127* (43), 12944–12948. https://doi.org/10.1002/ange.201504903.

(69) Kumar, K.; Dubau, L.; Mermoux, M.; Li, J.; Zitolo, A.; Nelayah, J.; Jaouen, F.; Maillard, F. On the Influence of Oxygen on the Degradation of Fe-N-C Catalysts. *Angewandte Chemie* **2020**, *132* (8), 3261–3269. https://doi.org/10.1002/ange.201912451.

(70) Choi, C. H.; Lim, H. K.; Chung, M. W.; Chon, G.; Ranjbar Sahraie, N.; Altin, A.; Sougrati, M. T.; Stievano, L.; Oh, H. S.; Park, E. S.; Luo, F.; Strasser, P.; Dražić, G.; Mayrhofer, K. J. J.; Kim, H.; Jaouen, F. The Achilles' Heel of Iron-Based Catalysts during Oxygen Reduction in an Acidic Medium. *Energy Environ Sci* **2018**, *11* (11), 3176–3182. https://doi.org/10.1039/c8ee01855c.

(71) Li, T.; Liu, J.; Song, Y.; Wang, F. Photochemical Solid-Phase Synthesis of Platinum Single Atoms on Nitrogen-Doped Carbon with High Loading as Bifunctional Catalysts for Hydrogen Evolution and Oxygen Reduction Reactions. *ACS Catal* **2018**, *8* (9), 8450–8458. https://doi.org/10.1021/acscatal.8b02288.

(72) Liu, Q.; Li, Y.; Zheng, L.; Shang, J.; Liu, X.; Yu, R.; Shui, J. Sequential Synthesis and Active-Site Coordination Principle of Precious Metal Single-Atom Catalysts for Oxygen Reduction Reaction and PEM Fuel Cells. *Adv Energy Mater* **2020**, *10* (20). https://doi.org/10.1002/aenm.202000689.

(73) Zhang, C.; Sha, J.; Fei, H.; Liu, M.; Yazdi, S.; Zhang, J.; Zhong, Q.; Zou, X.; Zhao, N.; Yu, H.; Jiang, Z.; Ringe, E.; Yakobson, B. I.; Dong, J.; Chen, D.; Tour, J. M. Single-Atomic Ruthenium Catalytic Sites on Nitrogen-Doped Graphene for Oxygen Reduction Reaction in Acidic Medium. *ACS Nano* **2017**, *11* (7), 6930–6941. https://doi.org/10.1021/acsnano.7b02148.

(74) Xiao, M.; Gao, L.; Wang, Y.; Wang, X.; Zhu, J.; Jin, Z.; Liu, C.; Chen, H.; Li, G.; Ge, J.; He, Q.; Wu, Z.; Chen, Z.; Xing, W. Engineering Energy Level of Metal Center: Ru Single-Atom Site for Efficient and Durable Oxygen Reduction Catalysis. *J Am Chem Soc* **2019**, *141* (50), 19800–19806. https://doi.org/10.1021/jacs.9b09234.

(75) Xie, X.; He, C.; Li, B.; He, Y.; Cullen, D. A.; Wegener, E. C.; Kropf, A. J.; Martinez, U.; Cheng, Y.; Engelhard, M. H.; Bowden, M. E.; Song, M.; Lemmon, T.; Li, X. S.; Nie, Z.; Liu, J.; Myers, D. J.; Zelenay, P.; Wang, G.; Wu, G.; Ramani, V.; Shao, Y. Performance Enhancement and Degradation Mechanism Identification of a Single-Atom Co–N–C Catalyst for Proton Exchange Membrane Fuel Cells. *Nat Catal* **2020**, *3* (12), 1044–1054. https://doi.org/10.1038/s41929-020-00546-1.

(76) Dong, H.; Gu, F.; Li, M.; Lin, B.; Si, Z.; Hou, T.; Yan, F.; Lee, S. T.; Li, Y. Improving the Alkaline Stability of Imidazolium Cations by Substitution. *ChemPhysChem* **2014**, *15* (14), 3006–3014. https://doi.org/10.1002/cphc.201402262.

(77) Hu, Y.; Jensen, J. O.; Pan, C.; Cleemann, L. N.; Shypunov, I.; Li, Q. Immunity of the Fe-N-C Catalysts to Electrolyte Adsorption: Phosphate but Not Perchloric Anions. *Appl Catal B* **2018**, *234*, 357–364. https://doi.org/10.1016/j.apcatb.2018.03.056.

(78) Elvington, M. C.; Chung, H. T.; Lin, L.; Yin, X.; Ganesan, P.; Zelenay, P.; Colón-Mercado, H. R. Communication—On the Lack of Correlation between the Voltammetric Redox Couple and ORR Activity of Fe-N-C Catalysts. *J Electrochem Soc* **2020**, *167* (13), 134510. https://doi.org/10.1149/1945-7111/abb97c.

(79) Shah, S. S. A.; Najam, T.; Javed, M. S.; Rahman, M. M.; Tsiakaras, P. Novel Mn-/Co-N x Moieties Captured in N-Doped Carbon Nanotubes for Enhanced Oxygen Reduction Activity and Stability in Acidic and Alkaline Media. *ACS Appl Mater Interfaces* **2021**, *13* (19), 23191–23200. https://doi.org/10.1021/acsami.1c03477.

(80) Tylus, U.; Jia, Q.; Strickland, K.; Ramaswamy, N.; Serov, A.; Atanassov, P.; Mukerjee, S. Elucidating Oxygen Reduction Active Sites in Pyrolyzed Metal-Nitrogen Coordinated Non-Precious-Metal Electrocatalyst Systems. *Journal of Physical Chemistry C* **2014**, *118* (17), 8999–9008. https://doi.org/10.1021/jp500781v.

(81) Zeng, J. S.; Corbin, N.; Williams, K.; Manthiram, K. Kinetic Analysis on the Role of Bicarbonate in Carbon Dioxide Electroreduction at Immobilized Cobalt Phthalocyanine. *ACS Catal* **2020**, *10* (7), 4326–4336. https://doi.org/10.1021/acscatal.9b05272.

(82) Yan, C.; Li, H.; Ye, Y.; Wu, H.; Cai, F.; Si, R.; Xiao, J.; Miao, S.; Xie, S.; Yang, F.; Li, Y.; Wang, G.; Bao, X. Coordinatively Unsaturated Nickel-Nitrogen Sites towards Selective and High-Rate CO2 Electroreduction. *Energy Environ Sci* **2018**, *11* (5), 1204–1210. https://doi.org/10.1039/c8ee00133b.

(83) Cheng, Y.; Zhao, S.; Li, H.; He, S.; Veder, J. P.; Johannessen, B.; Xiao, J.; Lu, S.; Pan, J.; Chisholm, M. F.; Yang, S. Z.; Liu, C.; Chen, J. G.; Jiang, S. P. Unsaturated Edge-Anchored Ni Single Atoms on Porous Microwave Exfoliated Graphene Oxide for Electrochemical CO2. *Appl Catal B* **2019**, *243* (June 2018), 294–303. https://doi.org/10.1016/j.apcatb.2018.10.046.

(84) Yang, J.; Qiu, Z.; Zhao, C.; Wei, W.; Chen, W.; Li, Z.; Qu, Y.; Dong, J.; Luo, J.; Li, Z.; Wu, Y. In Situ Thermal Atomization To Convert Supported Nickel Nanoparticles into Surface-Bound Nickel Single-Atom Catalysts. *Angewandte Chemie* **2018**, *130* (43), 14291–14296. https://doi.org/10.1002/ange.201808049.

(85) Vijay, S.; Gauthier, J. A.; Heenen, H. H.; Bukas, V. J.; Kristoffersen, H. H.; Chan, K. Dipole-Field Interactions Determine the CO2 Reduction Activity of 2D Fe–N–C Single-Atom Catalysts. *ACS Catal* **2020**, *10* (14), 7826–7835. https://doi.org/10.1021/acscatal.0c01375.

(86) Zhao, X.; Liu, Y. Origin of Selective Production of Hydrogen Peroxide by Electrochemical Oxygen Reduction. *J. Am. Chem. Soc.* **2021**, *143*, 9423.

(87) Li, J.; Liu, J.; Yang, B. Insights into the Adsorption/Desorption of CO2 and CO on Single-Atom Fe-Nitrogen-Graphene Catalyst under Electrochemical Environment. *Journal of Energy Chemistry* **2020**, *53*, 20–25. https://doi.org/10.1016/j.jechem.2020.04.016.

(88) Qin, X.; Vegge, T.; Hansen, H. A. CO2 Activation at Au(110)-Water Interfaces: An Ab Initio Molecular Dynamics Study. *Journal of Chemical Physics* **2021**, *155* (13). https://doi.org/10.1063/5.0066196.

(89) Cao, H.; Zhang, Z.; Chen, J.-W.; Wang, Y.-G. Potential-Dependent Free Energy Relationship in Interpreting the Electrochemical Performance of CO2 Reduction on Single Atom Catalysts. *ACS Catal* **2022**, *12* (11), 6606–6617. https://doi.org/10.1021/acscatal.2c01470.

(90) Alsunni, Y. A.; Alherz, A. W.; Musgrave, C. B. Electrocatalytic Reduction of CO2 to CO over Ag(110) and Cu(211) Modeled by Grand-Canonical Density Functional Theory. *Journal of Physical Chemistry C* **2021**, *125* (43), 23773–23783. https://doi.org/10.1021/acs.jpcc.1c07484.

(91) Sundararaman, R.; Goddard, W. A.; Arias, T. A. Grand Canonical Electronic Density-Functional Theory: Algorithms and Applications to Electrochemistry. *Journal of Chemical Physics* **2017**, *146* (11). https://doi.org/10.1063/1.4978411.

(92) Hutchison, P.; Rice, P. S.; Warburton, R. E.; Raugei, S.; Hammes-Schiffer, S. Multilevel Computational Studies Reveal the Importance of Axial Ligand for Oxygen Reduction Reaction on Fe–N–C Materials. *J Am Chem Soc* **2022**, *144* (36), 16524–16534. https://doi.org/10.1021/jacs.2c05779.

(93) Qian, S. J.; Cao, H.; Chen, J. W.; Chen, J. C.; Wang, Y. G.; Li, J. Critical Role of Explicit Inclusion of Solvent and Electrode Potential in the Electrochemical Description of Nitrogen Reduction. *ACS Catal* **2022**, *12* (18), 11530–11540. https://doi.org/10.1021/acscatal.2c03186.

(94) Zhao, X.; Liu, Y. Unveiling the Active Structure of Single Nickel Atom Catalysis: Critical Roles of Charge Capacity and Hydrogen Bonding. *J Am Chem Soc* **2020**, *142* (12), 5773–5777. https://doi.org/10.1021/jacs.9b13872.

(95) Zhao, X.; Liu, Y. Origin of Selective Production of Hydrogen Peroxide by Electrochemical Oxygen Reduction. *J. Am. Chem. Soc.* **2021**, *143*, 9423.

(96) Sebastián-Pascual, P.; Petersen, A. S.; Bagger, A.; Rossmeisl, J.; Escudero-Escribano, M. PH and Anion Effects on Cu-Phosphate Interfaces for CO Electroreduction. *ACS Catal* **2021**, *11* (3), 1128–1135. https://doi.org/10.1021/acscatal.0c03998.

(97) Stenlid, J. H.; dos Santos, E. C.; Bagger, A.; Johansson, A. J.; Rossmeisl, J.; Pettersson, L. G. M. Electrochemical Interface during Corrosion of Copper in Anoxic Sulfide-Containing Groundwater—A Computational Study. *The Journal of Physical Chemistry C* **2020**, *124* (1), 469–481. https://doi.org/10.1021/acs.jpcc.9b08657.

(98) Zhang, H.; Hwang, S.; Wang, M.; Feng, Z.; Karakalos, S.; Luo, L.; Qiao, Z.; Xie, X.; Wang, C.; Su, D.; Shao, Y.; Wu, G. Single Atomic Iron Catalysts for Oxygen Reduction in Acidic Media: Particle Size Control and Thermal Activation. *J Am Chem Soc* **2017**, *139* (40), 14143–14149. https://doi.org/10.1021/jacs.7b06514.

(99) Li, J.; Chen, M.; Cullen, D. A.; Hwang, S.; Wang, M.; Li, B.; Liu, K.; Karakalos, S.; Lucero, M.; Zhang, H.; Lei, C.; Xu, H.; Sterbinsky, G. E.; Feng, Z.; Su, D.; More, K. L.; Wang, G.; Wang, Z.; Wu, G. Atomically Dispersed Manganese Catalysts for Oxygen Reduction in Proton-Exchange Membrane Fuel Cells. *Nat Catal* **2018**, *1* (12), 935–945. https://doi.org/10.1038/s41929-018-0164-8.

(100) Luo, F.; Roy, A.; Silvioli, L.; Cullen, D. A.; Zitolo, A.; Sougrati, M. T.; Oguz, I. C.; Mineva, T.; Teschner, D.; Wagner, S.; Wen, J.; Dionigi, F.; Kramm, U. I.; Rossmeisl, J.; Jaouen, F.; Strasser, P. P-Block Single-Metal-Site Tin/Nitrogen-Doped Carbon Fuel Cell Cathode Catalyst for Oxygen Reduction Reaction. *Nat Mater* **2020**, *19* (11), 1215–1223. https://doi.org/10.1038/s41563-020-0717-5.

(101) Wang, T.; Cao, X.; Qin, H.; Shang, L.; Zheng, S.; Fang, F.; Jiao, L. P-Block Atomically Dispersed Antimony Catalyst for Highly Efficient Oxygen Reduction Reaction. *Angewandte Chemie - International Edition* **2021**, *60* (39), 21237–21241. https://doi.org/10.1002/anie.202108599.

(102) Bagger, A.; Ju, W.; Varela, A. S.; Strasser, P.; Rossmeisl, J. Electrochemical CO2 Reduction: A Classification Problem. *ChemPhysChem* **2017**, *18* (22), 3266–3273. https://doi.org/10.1002/cphc.201700736.

(103) Bagger, A.; Ju, W.; Varela, A. S.; Strasser, P.; Rossmeisl, J. Single Site Porphyrine-like Structures Advantages over Metals for Selective Electrochemical CO2 Reduction. *Catal Today* **2017**, *288*, 74–78. https://doi.org/10.1016/j.cattod.2017.02.028.